Metabolism 172 (2025) 156358

Contents lists available at ScienceDirect

Metabolism

journal homepage: www.journals.elsevier.com/metabolism

A key role of polyamine metabolism in adipose tissue homeostasis that regulates obesity

Christine Mund [a,1], Anupam Sinha [a,1], Anika Aderhold [a,1], Ivona Mateska [a], Eman Hagag [a], Sofia Traikov [a], Bettina Gercken [a], Andres Soto [a], Jonathan Pollock [b], Lilli Arndt [c], Michele Wölk [d], Natalie Werner [d], Georgia Fodelianaki [a], Pallavi Subramanian [a], Kyoung-Jin Chung [a], Sylvia Grossklaus [a], Mathias Langner [a], Mohamed Elgendy [a], Tatyana Grinenko [a], Ben Wielockx [a], Andreas Dahl [e], Martin Gericke [c], Matthias Blüher [f], Ünal Coskun [d,g,h], David Voehringer [b], Maria Fedorova [d], Mirko Peitzsch [a], Peter J. Murray [i,1], Triantafyllos Chavakis [a,g,h,1], Vasileia Ismini Alexaki [a,*]

[a] Institute for Clinical Chemistry and Laboratory Medicine, Faculty of Medicine and University Hospital Carl Gustav Carus, Technische Universität Dresden, Dresden, Germany
[b] Department of Infection Biology, Universitätsklinikum Erlangen and Friedrich-Alexander, University Erlangen-Nürnberg, Erlangen, Germany
[c] Institute of Anatomy, Leipzig University, Leipzig, Germany
[d] Center of Membrane Biochemistry and Lipid Research, Faculty of Medicine, Technische Universität Dresden, Dresden, Germany
[e] DRESDEN-concept Genome Center, Center for Molecular and Cellular Bioengineering, Technische Universität Dresden, Dresden, Germany
[f] Clinic and Policlinic for Endocrinology and Nephrology, Medical Research Center, Universitätsmedizin Leipzig, Germany
[g] Paul Langerhans Institute Dresden of the Helmholtz Center Munich, University Hospital and Faculty of Medicine, TU Dresden, Dresden, Germany
[h] German Center for Diabetes Research (DZD), Neuherberg, Germany
[i] Max Planck Institute of Biochemistry, Martinsried, Germany

ARTICLE INFO

Keywords:
AZIN2
Polyamine metabolism
Adipocyte progenitors
Adipose tissue
Obesity

ABSTRACT

Background and aims: Adipose tissue function is integral to systemic metabolic homeostasis. Excessive adipose tissue growth is associated with development of chronic low-grade inflammation and whole body dysmetabolism. The cell metabolic pathways regulating adipose tissue growth and homeostasis are little understood. Here we studied the role of polyamine metabolism in adipose tissue (patho)physiology.
Methods: We generated mice with global and adipocyte progenitor (AP)-specific Antizyme inhibitor 2 (AZIN2) deficiency and performed diet-induced obesity studies. APs were isolated from the subcutaneous and gonadal adipose tissue of mice and cultured.
Results: Polyamine metabolism components, including AZIN2, were highly expressed in APs and their expression in the adipose tissue was downregulated with obesity. IL4 induced *Azin2* expression in APs. AZIN2 facilitated polyamine synthesis and acetylation, and regulated total acetyl-CoA levels in APs. AZIN2 deficiency upregulated histone acetylation in genes related to lipid metabolism. *Azin2*$^{-/-}$ APs committed more efficiently to adipogenesis in vivo and in vitro, and were more prone to senescence compared to wild-type counterparts. Upon diet-induced obesity, global and AP-specific AZIN2 deficiency in mice provoked AP depletion, adipocyte hypertrophy, obesity, inflammation, glucose intolerance and insulin resistance. In human adipose tissue, *AZIN2* expression strongly correlated with expression of progenitor markers.
Conclusions: Altogether, we identified AZIN2 as a novel AP marker that regulates AP fate and preserves adipose tissue health.

* Corresponding author at: Institute for Clinical Chemistry and Laboratory Medicine, Faculty of Medicine and University Clinic Carl Gustav Carus, Technische Universität Dresden, Fetscherstrasse 74, Dresden 01307, Germany.
E-mail address: VasileiaIsmini.Alexaki@uniklinikum-dresden.de (V.I. Alexaki).
[1] Equal contribution.

https://doi.org/10.1016/j.metabol.2025.156358
Received 7 April 2025; Accepted 22 July 2025
Available online 5 August 2025

1. Introduction

Obesity promotes development of type 2 diabetes, fatty liver disease, and cardiovascular disease [1]. Although the ability of adipocytes to sequester fat protects other organs from lipotoxicity [2], the excessive expansion of adipose tissue, leading to hypoxia and cell destruction, is associated with development of chronic low-grade inflammation and whole body dysmetabolism [3,4]. Adipose tissue growth is driven by the increase in size (hypertrophy) and number (hyperplasia) of adipocytes [2]. Although adipose tissue hyperplasia is associated with metabolic advantages compared to adipose tissue hypertrophy in established obesity [4], adipogenesis (generation of new adipocytes from progenitors) occurring at the start of high-fat diet (HFD) feeding enables adipose tissue expansion and thereby facilitates development of obesity [5–10].

New adipocytes emerge from platelet-derived growth factor-α positive (PDGFRα^{+}) progenitors [11,12]. Single-cell transcriptomic studies revealed different subpopulations of APs in human and mouse adipose tissue with variable adipogenic capacity [13–17]. The molecular path to de novo adipogenesis from APs is controlled in part by CCAAT-enhancer-binding protein β (C/EBPβ), C/EBPδ, and Peroxisome Proliferator-Activated Receptor γ (PPARγ), leading to accumulation of lipid droplets that gradually merge to form mature adipocytes [4,18], which further increase in size by triglyceride (TG) storage. Although the transcriptional regulation of adipogenesis has been deciphered in detail [18], its regulation by metabolic pathways remains largely unknown.

Polyamines are present in all life kingdoms [19]. As polycations, they bind to negatively charged molecules, such as DNA, RNA or phospholipids, and have broad functions in cellular homeostasis and division [20–25]. Polyamine amounts are regulated by de novo biosynthesis (from arginine, proline or glutamine), recycling and uptake by transporters [26,27]. Arginine is metabolized through arginase (ARG) 1 or 2 to L-ornithine, which is further metabolized by ornithine decarboxylase 1 (ODC1) to putrescine; this is the rate-limiting step of the de novo polyamine biosynthesis pathway. Putrescine is converted to spermidine by spermidine synthase (SRM), and spermidine is used by spermine synthase (SMS) to produce spermine [20]. In recycling reactions, spermine can regenerate spermidine via spermine oxidase (SMOX). Spermidine is acetylated by spermidine/spermine-N1-acetyltransferase (SAT1) to N1-acetyl-spermidine, which is oxidized by polyamine oxidase (PAOX) to regenerate putrescine [28]. Polyamine synthesis is primarily regulated at the level of ODC1 by antizymes, which physically interact with ODC1 to inhibit its activity and stimulating its ubiquitin-independent proteasomal degradation [25,26]. In turn, AZs are themselves regulated by antizyme inhibitors (AZIN1 and 2), which are structurally similar to ODC1 but enzymatically inactive and titrate AZs, freeing ODC1 to form active homodimers [29,30]. Thus, AZIN1 and AZIN2 by virtue of their ability to inhibit the inhibitors, are positive regulators of ODC1.

Polyamines were recently shown to regulate adipose tissue homeostasis [27,31–35]. Endothelial cell-derived polyamines promote lipolysis in adipocytes in a paracrine manner freeing fatty acids, which are taken up and oxidized by endothelial cells to support their proliferation [32]. Furthermore, spermidine supplementation reduces adiposity and adipose tissue inflammation, improves glucose homeostasis and increases brown adipose tissue thermogenesis [33–35]. We demonstrate here that polyamine metabolism plays a profound role particularly in APs. Numerous components of polyamine metabolism are expressed in APs and their expression in adipose tissue is downregulated in obesity. Among them, we found that AZIN2 is highly expressed in APs and that it is a key regulator of adipogenesis. AZIN2 promotes polyamine synthesis and acetylation, leading to decreased acetyl-CoA amounts, and negatively regulates histone acetylation marks in regulatory elements of adipogenic genes in APs. Young chow diet (CD)-fed *Azin2*$^{-/-}$ mice display increased adipogenesis and reduced AP proliferation leading to AP depletion. Upon HFD feeding, *Azin2*$^{-/-}$ mice or mice with inducible AP-specific AZIN2 deficiency develop enlarged adipose tissue with enhanced inflammation compared to wild-type (wt) mice, indicating that AZIN2-driven polyamine metabolism in APs is critical for maintaining adipose tissue health. In sum, AZIN2-driven polyamine metabolism emerges as a potent regulator of adipose tissue homeostasis.

2. Materials and methods

2.1. Mice

For the generation of *Azin2*$^{-/-}$ mice, zygotes were isolated from superovulated female C57Bl/6NCrl mice at E0.5. Single zygotes were microinjected with Cas9 RNPs prepared from 333.3 ng/μl NLS-Cas9 (ToolGen), 1 μM gRNA1 (5′TCAGCGACGCCCCAAACCTC3′), 1 μM gRNA2 (5′GAGGGCGGCGGCACATTCAC3′), and 2 μM tracrRNA (Integrated DNA Technologies). Embryos that developed to the two-cell stage were transferred into pseudopregnant foster mothers. *Azin2*$^{-/-}$ mice carried deletion of *Azin2* exons 6 to 9. PCR genotyping was used to identify founders with mutated alleles. PCR genotyping was performed using following primers for the *Azin2*$^{-/-}$ Fw 5′ACCTGCCTGGTATGGAGTTG3′, Rv 5′GTGCCTCTGCCTCCTAAGTG3′ (product size 575 bp) or Fw 5′CGGAGTCCAAAGAAAGAGC3′ and Rv 5′GAACACAGCTCGGTGACAGT3′(product size 257 bp). For wt mice following primers were used: Fw 5′GCTCTTCCTCCTTTCCCAGT3′, Rv 5′CCACGCTTGACCACACATTA3′ (product band size 206 bp).

Azin2$^{fl/fl}$ mice were generated by Ozgene ARC. Briefly, exon 7 of the *Azin2* gene was flanked by loxP sites. Breeding to flp removed the neo cassette generating a conditional floxed allele. Breeding to Cre removed exon 7 to introduce a translational frameshift rendering downstream exons non-functional. PCR genotyping was performed using following primers: Fw 5′ TATCCCCAAAAGGTTTCTCTCCAG3′, Rv 5′ATCTGAAACACCAGCCTAGCATC3′, which generated a 256 bp product in wt and a 365 bp product in floxed alleles.

Pdgfra^{CreER} mice were purchased from The Jackson Laboratory (B6N.Cg-Tg(Pdgfra-cre/ERT)467Dbe/J, #:018280). *Azin2*^{APKO} (*Pdgfra*$^{Cre+Er}$;*Azin2*$^{fl/fl}$) and *Azin2*$^{fl/fl}$ (*Pdgfra*$^{Cre-Er}$;*Azin2*$^{fl/fl}$) were generated by crossing *Pdgfra*$^{Cre+Er}$ mice with *Azin2*$^{fl/fl}$ mice.

2.2. In vivo experiments

All feedings were performed in male mice and were started at the age of 6–7 weeks. C57BL/6J wt male mice were fed for 20 weeks a low-fat diet (LFD, 10 % of kcal from fat, D12450B, Research Diets) or a HFD (60 % of kcal from fat, D12492, Research Diets). Male *Azin2*$^{-/-}$ and wt littermates were fed for 8 weeks a LFD or a HFD. BrdU pulse-chase experiments were performed in male *Azin2*$^{-/-}$ and wt littermate mice fed for 8 weeks a HFD and treated during the first feeding week with BrdU (0.8 mg/ml in the drinking water), as previously described [6]. AP-specific gene deletion was induced in *Pdgfra*^{CreER};*Azin2*$^{fl/fl}$ male mice by tamoxifen (100 mg/kg body weight, ARISTO Pharma GmbH) given via oral gavage (o.g.) at 5 consecutive days diluted in SMOFlipid lipid emulsion solution (Fresenius Kabi Deutschland GmbH) followed by 3.5 weeks of feeding with HFD containing 400 mg/kg tamoxifen. Afterwards, the mice were fed another 5 weeks with HFD. The body weight was measured every week during the course of the feeding. For glucose tolerance (GTT) mice were fasted overnight and then were intraperitoneally (i.p.) injected with D-(+)-glucose (Sigma Aldrich) (1 g/kg of body weight). For insulin tolerance tests (ITT), after 6 h fasting 0.5 or 1 U/kg insulin (Eli Lilly and Company) was i.p. injected in lean and obese mice, respectively. Blood glucose levels were measured via the tail vein with an Accu-Chek glucosemeter (Roche) at 0, 15, 30, 60, 90 and 120 min [36,37]. The metabolic profile of mice was analyzed in metabolic cages as previously described [36]. Briefly, mice of similar weights were individually housed in metabolic cages (PhenoMaster, TSE Systems) for 3 days with free access to water and food maintaining a 12 h:12 h light/dark cycle. A period of at least 24 h acclimatization in the metabolic

cages preceded initiation of the experiment and data collection. Volume of oxygen consumption (VO_2), carbon dioxide production (VCO_2), food intake and locomotion were determined every 20 min. Energy expenditure (EE) was calculated as $3.941 \times VO_2 + 1.106 \times VCO_2$.

For IL4 treatments mice were fed for 6 weeks a HFD and during the last 2 weeks of HFD feeding they were i.p. injected every second day with a complex of mouse recombinant IL4 (2 μg/mouse) (Peprotech) and anti-IL4 (10 μg/mouse) (Tonbo Biosciences) diluted in PBS, as previously described [38,39]. Control mice received equal volume of PBS i.p. injections.

Mice were injected with 500 L3-stage *N. brasiliensis* larvae subcutaneously and analyzed 9 days later, as previously described [40].

At the end of the experiments, inguinal subcutaneous (SAT), gonadal (GAT), axillary, mesenteric, perirenal, retroperitoneal and brown adipose tissue (BAT) were collected, weighed and either snap-frozen or further processed for stromal vascular fraction (SVF) or adipocyte fraction (AF) isolation or cell sorting. To determine the lean mass the sum of the weights of all aforementioned adipose tissues (total fat mass) was subtracted from the body weight. Animal experiments were approved by the Landesdirektion Sachsen, Germany, the Regierung von Mittelfranken, Germany and the Bezirksregierung Leipzig, Bezirksregierung Halle, Germany.

2.3. Cell isolation and culture, and explant culture

For AP isolation, SAT and GAT were harvested, minced on ice and incubated for 45 min with collagenase type I (Thermo Fisher Scientific) (2 mg/ml/g tissue) at 37 °C under continuous rotation. Cells were then passed through a 100-μm pore-sized cell strainer and centrifuged at 300*g* for 10 min. In some experiments the floating AF was collected. Erythrocytes were removed from the SVF through lysis with a red blood cell (RBC) lysis buffer (Biolegend) and SVF cells were used for RNA isolation, FACS analysis or AP sorting. APs were sorted by FACS as $PDGFR\alpha^+LY6A^+CD31^-CD45^-$ cells with a BD FACS ARIA apparatus (BD Biosciences) and using the BD FACSDIVA v8.0.1 software (BD Biosciences) [36] or as $CD31^-CD45^-$ cells using anti-CD31 and anti-CD45 MicroBeads (Miltenyi Biotec), according to manufacturer's instructions. $CD31^+$ and $CD45^+$ cells were also kept and analyzed. In some experiments $CD11b^-$ cells were isolated from SAT SVF with anti-CD11b MicroBeads (Miltenyi Biotec). Adipose tissue myeloid cells (ATMCs) were isolated as $CD11b^+CD45^+$ cells from SAT of mice fed for 20 weeks a HFD using anti-CD11b and anti-CD45 MicroBeads (Miltenyi Biotec). Hepatocytes were isolated as previously described [41].

APs were grown for one week in 4.5 g/l glucose Glutamax–DMEM with 10 % FBS and 1 % penicillin/streptomycin at 37 °C and 5 % CO_2. For adipogenic differentiation they were cultured in medium containing 5 μg/ml insulin (Sigma-Aldrich), 0.5 mM 3-isobutyl-1-methylxantine (Sigma-Aldrich), 1 μM dexamethasone (Sigma-Aldrich) and 1 μM rosiglitazone (Sigma-Aldrich). After 2 days, they were switched to medium containing 5 μg/ml insulin and cultured for another 5 days. Medium was changed every 2 days. To study senescence, APs were differentiated for one week and cultured for another week in culture medium.

SAT or GAT explants from *Azin2*$^{-/-}$, *Il4ra*$^{-/-}$ and their respective wt littermate control mice were isolated, minced and kept for 18 h in 5 g/l glucose Glutamax – supplemented DMEM with 1 % FBS and 1 % penicillin/streptomycin at 37 °C and 5 % CO_2.

3T3-L1 pre-adipocytes (CL-173, ATCC) were maintained in 4.5 g/l glucose Glutamax – supplemented DMEM with 10 % FBS and 1 % penicillin/streptomycin at 37 °C and 5 % CO_2. 3T3-L1 cells were tested Mycoplasma free.

Human pre-adipocytes (P10761, Innoprot) were cultured for up to 3 passages in preadipocyte medium containing 1 % preadipocyte growth supplement, 5 % FBS and 1 % penicillin/streptomycin (Innoprot) at 37 °C and 5 % CO_2 on cell culture plates pre-coated with 2 μg/cm^2 poly-L-lysine. For differentiation, they were cultured for 2 days in differentiation medium containing 1 % preadipocyte differentiation supplement, 5 % FBS and 1 % penicillin/streptomycin and for another 6 days in preadipocyte medium containing 0.5 mg/ml insulin.

2.4. Cell and explant treatments

Undifferentiated APs were treated for 4 or 24 h with mouse recombinant IL4 or IL13 (both at 20 ng/ml, purchased from PeproTech) in 1 % FBS 4.5 g/l glucose Glutamax – supplemented DMEM. Undifferentiated human preadipocytes were treated for 24 h with 12 ng/ml human recombinant IL4 (PeproTech). Undifferentiated APs were also treated for 24 h with putrescine, spermidine or spermine (all 10 μM, Sigma-Aldrich) in 1 % FBS 4.5 g/l glucose Glutamax – supplemented DMEM. In some experiments, APs were treated during 7-days differentiation with 10 μM spermidine (Sigma-Aldrich), 4 μM C646 (Sigma-Aldrich) or respective controls. All agents were re-added every 2 days with fresh medium. For arginine metabolite measurement, cells were starved for 2 h in Silac medium (Thermo Fisher Scientific) without FBS containing 146 mg/l L-lysine (Sigma-Aldrich), then 400 μM arginine (Sigma-Aldrich) was added and cell lysates or supernatants were collected after 60 min.

2.5. siRNA transfections

Undifferentiated APs were transfected with TARGETplus SMARTpool siRNA against *Azin2*, *Slc7a2*, *Arg1*, *Sat1*, *Odc1*, *Stat6* or control non-targeting siRNA (all at 30 nM and from Horizon Discovery) using Lipofectamine RNAiMAX transfection reagent (Thermo Fisher Scientific) and the reverse transfection method per manufacturer's instructions. During differentiation, siRNA transfections were repeated every 2–3 days using same siRNA concentration and Lipofectamine volume.

2.6. Plasmid transfection

3T3-L1 cells were transfected with a plasmid overexpressing Myc-DDK tagged AZIN2 (NM_172875, mouse tagged ORF clone, Origene) or pCMV control plasmid using Lipofectamine LTX Reagent (Thermo Fisher Scientific) according to manufacturer's instructions and as previously described [42].

2.7. Bulk RNA-seq

Bulk RNA-seq was performed and analyzed as previously described [43,44]. For transcriptome mapping, strand-specific paired-end sequencing libraries from total RNA were constructed using TruSeq stranded Total RNA kit (Illumina Inc). Sequencing was performed on an Illumina HiSeq3000 (1 × 75 basepairs). Low quality nucleotides were removed with the Illumina fastq filter and reads were further subjected to adaptor trimming using cutadapt [45]. Alignment of the reads to the mouse genome was done using STAR Aligner [46] using the parameters: "–runMode alignReads –outSAMstrandField intronMotif –outSAMtype BAM SortedByCoordinate –readFilesCommand zcat". Mouse Genome version GRCm38 (release M12 GENCODE) was used for the alignment. The parameters: 'htseq-count -f bam -s reverse -m union -a 20', HTSeq-0.6.1p1 [47] were used to count the reads that map to the genes in the aligned sample files. The GTF file (gencode.vM12.annotation.gtf) used for read quantification was downloaded from Gencode (https://www.gencodegenes.org/mouse/release_M12.html). Gene centric differential expression analysis was performed using DESeq2_1.8.1 [48]. The raw read counts for the genes across the samples were normalized using 'rlog' command of DESeq2 and subsequently these values were used to render a PCA plot using ggplot2_1.0.1 [49].

Pathway and functional analyses were performed using GSEA [49] and EGSEA [50]. GSEA is a stand-alone software with a graphical user interface (GUI). To run GSEA, a ranked list of all the genes from DESeq2 based calculations was created using the −log10 of the *p*-value. This ranked list was then queried against Molecular Signatures Database (MsigDB), KEGG, GO, Reactome and Hallmark based repositories.

EGSEA is an R/Bioconductor based command-line package. For pathway analysis with EGSEA lists of DEG with padj <0.05 or $p < 0.05$ were used based on the KEGG database repository. For constructing heatmaps, the "rlog-normalized" expression values of the significantly expressed genes (padj <0.05) was scaled using z-transformation. The resulting matrices were visually rendered using MORPHEUS [43,44].

2.8. scRNA-seq

$CD45^{-}CD31^{-}$ SVF cells were isolated by negative selection with MicroBeads (Miltenyi Biotec) from SAT of *Azin2*$^{-/-}$ and wt mice (2 mice pooled per genotype) fed for 8 weeks a HFD. 10,275 wt and 11,004 *Azin2*$^{-/-}$ cells were subjected to droplet-based scRNA-seq. Specifically, the sorted cells were concentrated by centrifugation (300 rcf, 5 min, 4 °C) and the volume was reduced to 42 µl. Cells were carefully resuspended, cell concentration and quality was determined and cells were added to the reverse transcription mix before loading cells on the 10× Genomics Chromium system in a Chromium Single Cell G Chip and processed further following the guidelines of the 10× Genomics user manual (v3.1). In short, the droplets were directly subjected to reverse transcription, the emulsion was broken and cDNA was purified using Silane beads. After the amplification of cDNA with 11 cycles, it underwent 0.6× SPRI bead purification and quantification. The 10× Genomics scRNA-seq library preparation – involving fragmentation, dA-Tailing, adapter ligation and a 12 cycles indexing PCR – was performed with 25 % of the cDNA material based on the manufacturer's protocol. After quantification, the libraries were sequenced on an Illumina Novaseq6000 in paired-end mode (R1/R2: 100 cycles; I1/I2: 10 cycles), thus generating ~300 million fragment pairs. The raw sequencing data was then processed with the 'count' command of the Cell Ranger software (v6.1.2) provided by 10× Genomics with the option '–expect-cells' set to 10,000 (all other options were used as per default). To build the reference for Cell Ranger, mouse genome (GRCm39) as well as gene annotation (Ensembl 104) were downloaded from Ensembl. Genome and annotation were processed following the build steps provided by 10× (https://support.10xgenomics.com/single-cell-gene-expression/software/release-notes/build#mm10_2020A) to build the appropriate Cellranger reference.

Seurat (v 4.3.0) [51] was used to perform analyses of the scRNA-seq data in R (v 4.0.2) environment. Briefly, wt sample (10,275 cells and 17,032 genes) and *Azin2*$^{-/-}$ sample (11,004 cells and 17,476 genes) were analyzed using the SCTransform command (running on parameters: vst.flavor = "v2", verbose = FALSE, ncells = 10,000, variable.features. n = 6,000). Subsequently, RunPCA, RunUMAP and FindNeighbors commands were run using 50 dimensions. A "resolution" of 0.07 was used to run FindClusters command. The resultant Seurat "objects" were integrated as described on https://satijalab.org/seurat/articles/sctransform_vignette. The numbers of features and dimensions used were same as above. The "resolution" was set to 0.03. NormalizeData was used to perform normalization on the integrated dataset with normalization.method set to "LogNormalize" and scale.factor set to 10,000. FindVariableFeatures, with "selection.method" set to "vst" and number of features limited to 6,000 was used to find the most variable genes. ScaleData command was then used to run the Seurat object using the variable features found in the previous step. Subsequently, "FindMarkers" command was used to find the differentially expressed genes, with logfc.threshold set to 0.1., between the *Azin2*$^{-/-}$ and wt cells. The R package enrichR (which provides an API to https://maayanlab.cloud/Enrichr/ webserver [52]) was used to perform functional analyses of the differentially expressed genes. Plotting was done using the functions from Seurat and ggplot2.

2.9. ChIP-qPCR

ChIP was performed using the EZ-Magna ChIP HiSens (Millipore) following manufacturer's instructions. Briefly, differentiated APs were cross-linked using 1 % formaldehyde for 10 min at room temperature (RT) and quenched with glycine. Chromatin shearing was achieved by sonication for 25 cycles (20 s on and 20 s off) on wet ice to generate DNA fragments with average length of 200–500 bp. Five µl of sheared cross-linked chromatin were kept to be used as 100 % input. Immunoprecipitation was performed by incubating the sheared chromatin with the magna ChIP protein A/G magnetic beads and the antibody either against H3K27Ac (Millipore 17-683), H3K9Ac (Millipore 17-658) or IgG control antibody overnight at 4 °C. Histone acetylation of *Pparg2* promoter was assessed by qPCR using the following primers: F 5′TGTGTGGGTCACTGGCGAGACA3′; R 5′TGGCTGGCACTGTCCTGACTGA3′ and the SsoFast Eva Green Supermix (Bio-Rad, Munich, Germany), a CFX384 real-time System C1000 Thermal Cycler (Bio-Rad) and the Bio-Rad CFX Manager 3.1 software.

2.10. Bulk ChIP-seq

For ChIP-seq, libraries were generated using the NEBNext Ultra II DNA library Prep kit (Illumina Inc). Nextflow (v 22.02.1) [53] was used to run the nf-core/chipseq: 2.0.0 workflow pipeline (https://nf-co.re/chipseq) with the following parameters: –genome GRCm38 –macs_pvalue 0.1 –max_cpus 4 –macs_gsize 1.87e9. The "narrowPeak" files generated from the pipeline were further numerically sorted by the region coordinates and then merged (using the "merge" function from bedtools v2.17.0 [54]) to create a consensus bed file. This file was subsequently used along with "featureCounts" [55] (running on parameters: isPairedEnd = TRUE, checkFragLength = TRUE, requireBothEndsMapped = TRUE) to create counts matrix for all the samples. Normalization and differential analyses were performed using DESeq2. [48] Functional annotation of the differentially activated regions was done using g:Profiler webserver [56]. Figures were plotted using ggplot2 in R environment [49]. "bigwig" files were used to visualize genomic regions in IGV [57]. Following commands from Deeptools package [58] executed sequentially using the listed respective parameters to generate the profile and heatmap plots for the ChIP-Seq data: 1) bamCompare –binSize 20 –normalizeUsing BPM –smoothLength 60 –extendReads 150 –centerReads –scaleFactorsMethod None 2) computeMatrix scale-regions –beforeRegionStartLength 5,000 –regionBodyLength 5,000 –afterRegionStartLength 5,000 –skipZeros (a bed file listing the differentially activated regions were provided) 3) plotProfile –perGroup red red red blue blue blue -out –samplesLabel "KO1" "KO2" "KO3" "WT1" "WT2" "WT3" –refPointLabel "TSS" –yAxisLabel "Average Signal Intensity" 4) plotHeatmap2 -samplesLabel "KO1" "KO2" "KO3" "WT1" "WT2" "WT3" –regionsLabel "Genome-Wide Assay Signal at Genes" –yAxisLabel "Fold Enrichment (Average Log2 IP/Input)" –zMax 0.5 –legendLocation none.

2.11. Arginine metabolite measurement

Arginine and its metabolites ornithine, putrescine, spermidine, spermine, N1-acetylspermidine, and N1-acetylspermine were measured by liquid chromatography-tandem mass spectrometry (LC-MS/MS) as previously described [59]. In brief, cultured cells were washed with cold PBS and lysed in the culture plates using methanol/water (1/1) (200 µl per well in 24-well plates). Adipose tissue was homogenized in 200 µl acetonitrile/water (1/1) using a tissue grinder. Ten microliters of cell culture supernatant were mixed with 200 µl acetonitrile/water (1/1). Samples were vortex-mixed for 1 min and centrifuged at 3,000*g* for 10 min at 4 °C. Supernatants from extracted samples were transferred directly onto a 96-well polytetrafluoroethylene (PTFE)-filter plate (Merck-Millipore) and filtered by assistance of positive pressure. Subsequently, filtered extracts were dried in a vacuum-assisted centrifuge, thereafter reconstituted in 200 µl initial mobile phase and analyzed by LC-MS/MS.

2.12. Lipidomics

Lipids from approximately 50 mg adipose tissue were extracted as described [60] using SPLASH®Lipidomix® (Avanti Polar Lipids Inc.) as internal standard. Lipid extracts were dissolved in 300 µl chloroform (EMSURE ACS, ISO, Reag. Ph Eur; Supleco):methanol (ULC-MS grade, >99.97 %; Biosolve-Chemicals) (2:1, *v*/v), 10 µl of the extracts were dried in vacuum and reconstituted in 150 µl chloroform:2-propanol (ULC/MS-CC/SFC grade, >99.95 %; Biosolve-Chemicals) (1:1, v/v). Lipids (3 µl) were separated by reverse phase chromatography (Accucore C30 column; 150 mm × 2.1 mm 2.6 µM 150 Å, Thermo Fisher Scientific) using a Vanquish Horizon UHPLC system (Thermo Fisher Scientific) coupled on-line to a Orbitrap Exploris 240 mass spectrometer (Thermo Fisher Scientific) equipped with a HESI source. Lipids were separated at a flow rate of 0.3 ml/min (column temperature 50 °C) and the following gradient: 0–20 min 10 to 80 % B, 20–37 min 80 to 95 % B,37–41 min 95 to 100 % B,41–49 min 100 % B, 49.1–57 min 10 % B. Eluent A consisted of acetonitrile:water (50:50, v/v, both ULC/MS-CC/SFC grade, Biosolve-Chemicals) and Eluent B of 2-propanol:acetonitrile: water (85:10:5, v/v/v), both containing 5 mM ammonium formate (MS grade, Sigma-Aldrich) and 0.1 % formic acid (ULC/MS-CC/SFC grade, Biosolve-Chemicals). Full MS settings were the following: spray voltage – 3500 V, sheath gas – 40 arb units, aux gas – 10 arb units, sweep gas – 1 arb unit, ion transfer tube – 300 °C, vaporizer temperature – 370 °C, EASY-IC run-start, default charge state – 1, resolution at *m/z* 200–120.000, scan range – *m/z* 200–1200, normalized AGC target – 100 %, maximum injection time – auto, RF lens – 35 %. Data-dependent acquisition (DDA) was based on a cycle time (1.3 s) at a resolution of 30.000, isolation window – 1.2 *m/z*, normalized stepped collision energies – 17, 27, 37 %, AGC target – 100 %, maximum injection time – 54 ms.

Data analysis was performed using Lipostar2 [61]. Briefly, supersample filter considering only lipids with isotopic pattern and with a MS/MS spectrum were kept, detected features were searched against the LIPID MAPS structural database (downloaded 11/2021), and proposed identifications obtained by automatic approval considering 3 and 4 stars manually evaluated. Relative quantities were calculated based on the internal standards and obtained ratios to the extract tissue weight used for extraction.

2.13. Acetyl-CoA measurement

For acetyl-CoA measurement, cultured cells were washed with cold PBS, scraped on ice in cold PBS, centrifuged for 2 min at 1,500 rpm at 4 °C, washed once with 0.1 M ammonium bicarbonate and centrifuged again for 2 min at 1,500 rpm at 4 °C. Cell pellets and tissues were snap-frozen and kept at −80 °C until further analysis. Frozen samples were dissolved in 150 µl 30 % methanol in acetonitrile with 100 nM chloropropamide as internal standard. Adipose tissue samples were homogenized in 200 µl 80 % isopropanol, 0.5 mm zirconium beads (1/3 volume) were added, samples were homogenized for 15 min at 4 °C and 300 x g in a TissueLyser II (Qiagen) and centrifuged at 13,000 ×*g* for 30 min. Supernatants were collected to be analyzed by LC-MS/MS. For adipose tissue, the supernatant was twice extracted with 1 ml hexane to remove the bulk of di- and triacylglycerols and sterols [62]. The collected lower fraction was dried and re-dissolved in 200 µl acetonitrile. LC–MS/MS analysis was performed on high performance liquid chromatography (HPLC) system (Agilent 1200) coupled online to G2-S QTof (Waters). For normal phase chromatography Bridge Amide 3.5 µl (2.1 × 100 mm) columns (Waters) were used. For the normal phase the mobile phase composed of eluent A (95 % acetonitrile, 0.1 mM ammonium acetate, and 0.01 % NH_4OH) and eluent B (40 % acetonitrile, 0.1 mM ammonium acetate, and 0.01 % NH_4OH) was applied with the following gradient program: Eluent B, from 0 % to 100 % within 18 min; 100 % from 18 to 21 min; 0 % from 21 to 26 min. The flow rate was set at 0.3 ml/min. The spray voltage was set at 3.0 kV and the source temperature was set at 120 °C. Nitrogen was used as both cone gas (50 l/h) and desolvation gas (800 l/h), and argon as the collision gas. MSE mode was used in negative ionization polarity. Mass chromatograms and mass spectral data were acquired and processed by MassLynx software (Waters).

2.14. RNAscope

RNAscope was performed in adipose tissue using the RNAscope Multiplex Fluorescent v2 Assay combined with immunofluorescence per manufacturer's instructions. Snap-frozen SAT and GAT were formalin-fixed paraffin-embedded and cut in 5-µm thick slices. The slides were incubated for 1 h at 60 °C, dehydrated with Roti-clear (CarlRoth) 2 × 5 min and ethanol 2 × 2 min and incubated for 30 min at 60 °C and then 10 min with a H_2O_2 solution (ACD) at RT. Then, they were washed with distilled water, incubated for 15 min with CO-Detection Target Retrieval (ACD) using a pressure cook, rinsed with distilled water and washed 3 × 5 min with PBS-T. Antibodies anti-PDGFRα (1:200, AF1062, R&D Systems), anti-perilipin (1:100, GP29, Progen) or anti-caveolin (1:150, ab192869, Abcam) diluted in CO-Detection Buffer (ACD) were added overnight at 4 °C. Then, slides were washed 2 × 2 min with PBS-T and fixed with neutral buffered formalin (Morphisto GmbH) 30 min at RT, washed 2 × 2 min with PBS-T and incubated with Protease Plus (ACD) 15 min at 40 °C using the HybEZ II hybridization system oven (ACD). After washing with distilled water, the samples were let to hybridize for 2 h at 40 °C in the HybEZ II oven with the Probe-Mm-*Azin2* (569871, Bio-techne). The slides were then hybridized with Amplifier (AMP)1, AMP2 and AMP3 for 30 min at 40 °C in the HybEZ II oven with 2 × 2 min washes with ACD Wash Buffer in between hybridizations. Afterwards, slides were sequentially incubated with RNAscope Multiplex FL v2 HRP-C1, OPAL 570 (Akoya Biosciences) and RNAscope Multiplex FL v2 HRP Blocker, all for 15 min at 40 °C in the HybEZ II oven with washes with ACD Wash Buffer in between incubations. Then, samples were incubated for 30 min at RT with donkey anti-goat IgG, Alexa Fluor™ 647 (A21447, Thermo Fisher Scientific), goat anti-guinea pig IgG H&L Alexa Fluor® 488 (ab150185, Abcam) or donkey anti-rabbit Alexa Fluor® 488 (A21206, Invitrogen) diluted in CO-Detection AB Diluent (ACD). Finally, they were washed 2 × 2 min with PBS-T, DAPI (1:10,000, Sigma-Aldrich) and then TrueBlack Lipofuscin Quencher (Thermo Fisher Scientific) were added for 30 s, and slides were mounted with Prolong Gold Antifade Mountant (Thermo Fisher Scientific). Adipose tissue sections were imaged with a ZeissLSM880 microscope (Zeiss).

2.15. Immunofluorescence in adipose tissue

Immunofluerescent stainings were performed as previously described [43,44]. Snap-frozen SAT and GAT were formalin-fixed, paraffin-embedded and cut in 5-µm thick slices. They were dehydrated 3 × 5 min with Roticlear (Carlroth), sequential 5-min washings with ethanol 100, 95, 80 and 70 % ethanol solutions, and a 5-min wash with PBS. Antigen retrieval was performed for 10 min with Target Retrieval Solution, Citrate pH 6 (Agilent) using a pressure cooker, followed by permeabilization for 10 min in 0.1 % Triton X-100 in PBS, 3 × 5 min washes with PBS and blocking 2 h with Protein Block, Serum-Free (Agilent). Then, samples were incubated overnight at 4 °C with following primary antibodies: anti-Arginase 1 (1:50, BD Biosciences, 610709), anti-SAT1 (1:100, Novus Biologicals, B110-41622), anti-ODC1 (1:100, Biorbyt, orb228847), anti-IL4Rα (1:50, Biorbyt, orb337363), anti-PDGFRα (1:200, R&D Systems, AF1062), anti-Perilipin (1:100, Progen, GP29) or anti-BrdU (1:50, ab6326, Abcam) all diluted in Antibody Diluent (Agilent). After samples were washed 3 × 5 min with PBS they were incubated for 1.5 h with following secondary antibodies all diluted 1:350 in Antibody Diluent (Agilent) at RT: donkey anti-mouse IgG, Alexa Fluor™ 647 (A-31571, Thermo Fisher Scientific) (against anti-Arginase 1), donkey anti-rabbit, Alexa Fluor™ 647 (A-31573, Thermo Fisher Scientific) (against anti-ODC1, anti-SAT1 and anti-BrdU),

donkey anti-goat IgG, Alexa Fluor™ 555 (A-21432, Thermo Fisher Scientific) (against anti-PDGFRα) and goat anti-guinea pig IgG H&L Alexa Fluor® 488 (ab150185, Abcam) (against anti-Perilipin). Samples were then washed 3 × 5 min with PBS, incubated for 30 s with TrueBlack® Lipofuscin Autofluorescence Quencher (Biotium), washed 3 × 5 min with PBS, stained with DAPI (1:10,000, Sigma-Aldrich) and mounted with Fluoromount-G™ Mounting Medium (Thermo Fisher Scientific). Adipose tissue sections were imaged with a Zeiss LSM880 microscope.

2.16. Histology

Fresh tissues were excised, snap-frozen, fixed in 4 % paraformaldehyde and embedded in paraffin. For adipocyte size analysis, sections were stained with hematoxylin and eosin (H&E). Sections were imaged with a Zeiss LSM880 microscope or with the Zeiss Axioscan 7 slide scanner microscope. A plugin macro in FIJI software was used for quantification of adipocyte size and frequency distribution analysis [63].

F4/80 and uncoupling protein 1 (UCP1) staining was performed as previously described [37]. Briefly, sections were deparaffinized and antigen retrieval was performed by incubation with hot citrate buffer (pH 6). Samples were allowed to cool down and they were washed 3 × 5 min with PBS-T. Then, they were treated for 10 min with peroxidase block (Agilent, Dako). F4/80 staining required proteinase K (Sigma-Aldrich) treatment at 37 °C. For UCP1 staining, sections were incubated with pronase (Sigma-Aldrich) at 37 °C. Sections were permeabilized with 0.4 % Triton X-100 and blocked with normal serum (Vectastatin AB kit (rat), Vector Lab). Next, they were incubated with anti-F4/80 (1:125, NB:600-404, Novus Biologicals) or anti-UCP1 (1:150, ab10983, Abcam) in antibody diluent (Agilent, Dako) overnight at 4 °C. Thereafter, they were washed 2 × 5 min with PBS-T and incubated for 1 h at RT with secondary anti-rat IgG antibody (PI-9400-1 Vector Laboratories). The avidin-biotin complex was detected with the 3-amino-9-ethylcarbazole (AEC) peroxidase substrate kit (Vector Laboratories). Images were acquired with a Zeiss LSM880 microscope.

Liver tissues were embedded in OCT. Sections were fixed for 30 min in 4 % PFA, washed 3 × 5 min with PBS and stained for 1 h at 37 °C with the Nile Red Staining Kit (Abcam), followed by DAPI staining and mounting. Images were acquired with an Axio Observer Z1/7 inverted microscope with Apotome mode (Zeiss) at 10 x magnification and the ZEN 3.2 blue edition software.

2.17. Oil Red O staining

Differentiated APs were washed twice with PBS, fixed with 10 % formalin for 1 h, rinsed with distilled water, and stained for 1 h with Oil Red O dye (Sigma-Aldrich) in 60 % isopropanol. Then, they were thoroughly rinsed with distilled water and images were acquired at bright field with an Axio Observer Z1/7 inverted microscope with Apotome mode (Zeiss) and the ZEN 3.2 blue edition software. At least 5 view-fields were imaged per sample. The stain was extracted through incubation with 100 % isopropanol for 5 min. Absorbance was measured at 492 nm using a microplate reader (Biotek).

2.18. Immunofluorescence in cultured cells

Differentiated APs were cultured in 8-well chamber slides (Ibidi). For PPARG staining they were washed with PBS, fixed for 10 min with 4 % paraformaldehyde, washed 3 × 5 min with PBS and permeabilized for 10 min with 0.1 % Triton X-100 in PBS. Then, they were washed 3 × 5 min with PBS and incubated with Protein Block, Serum-Free for 1 h (Agilent, Dako). Next, they were incubated with anti-PPARG (1:100, #2443, Cell Signaling) overnight at 4 °C. Afterwards, they were washed again 3 × 5 min with PBS and incubated for 1.5 h at RT with donkey anti-rabbit-Alexa Fluor™ 555 (A-31572, Thermo Fisher Scientific) diluted 1:350 in antibody diluent (Agilent, Dako). Finally, they were washed 3 × 5 min with PBS, stained with DAPI and mounted. Images were acquired with an Axio Observer Z1/7 inverted microscope with Apotome mode (Zeiss) and the ZEN 3.2 blue edition software.

For CDKN2A and CDKN1A staining, cells were fixed for 10 min with 4 % paraformaldehyde at RT and 3× washed with PBS. Then, they were permeabilized for 6 min with 0.1 % Triton X-100 in PBS, washed 3 × 5 min washes with PBS and blocked for 1 h with Protein Block, Serum-Free (Agilent). Then, they were incubated overnight at 4 °C with anti-CDKN2A (1:100, ab211542, Abcam) or anti-CDKN1A (1:200, ab188224, Abcam) diluted in Antibody Diluent (Agilent). Afterwards, they were washed 3 × 5 min with PBS and incubated for 2 h with donkey anti-rabbit-Alexa Fluor™ 555 (1:350, A-31572, Thermo Fisher Scientific). Cells were washed 3 × 5 min with PBS, stained with DAPI (1:10,000, Sigma-Aldrich) and mounted with Fluoromount-G™ Mounting Medium (Thermo Fisher Scientific). Slides were imaged with a Zeiss LSM880.

2.19. Senescence β-galactosidase staining

Differentiated APs were stained with the Senescence β-Galactosidase Staining Kit (#9860 Cell Signaling) following manufacturer's instructions. Images were taken with an Axio Observer Z1/7 inverted microscope with Apotome mode (Zeiss) and the ZEN 3.2 blue edition software. At least 5 view-fields were imaged per sample.

2.20. Image acquisition and analysis

RNAscope and immunofluorescence images were acquired on a Zeiss LSM 880 inverted confocal microscope (Zeiss), illuminated with laser lines at 405 nm, 488 nm, 561 nm and 633 nm, and detected by two photomultiplier tube detectors. EC Plan-Neofluar objectives with 20× and 40× magnification, 0.8 or 1.30 numerical aperture and M27 thread, working with an oil immersion medium Immersol 518 F, were used. Laser power, photomultiplier gain and pinhole size were set for each antibody individually and kept constant for all image acquisitions. Images were acquired with the ZEN 2.3 black edition software. Image processing was performed with Imaris 9/10 (Bitplane AG) with Labkit Plugin. Channels were Median filtered (3x3x1) and DAPI/Perilipin channels were rendered using the Imaris "Surface" pipelines, to outline the nucleus and adipocyte cell body, respectively. Channels were contrast adapted by linear stretch using the same limits across a sample set to make intensities comparable. Maximum intensity projections (MIP) were computed and "Snapshot" was taken. Video files were created by the "Animation" function of Imaris. Images are shown in pseudocolor; the display color of the channels was set as to optimize clarity of merged images.

Microscopic images of H&E stainings were acquired with an Axio Observer Z1/7 inverted microscope (Zeiss), on a Plan-Apochromat objective with 10× magnification, 0.30 numerical aperture and M27 thread. For each mouse at least 8 view-fields were imaged per tissue section. For imaging of whole adipose tissue sections following anti-BrdU staining in SAT of *Azin2*$^{-/-}$ and wt mice, and H&E staining in SAT of *Azin2*^{APKO} and *Azin2*$^{fl/fl}$ mice, a Zeiss Axioscan 7 slide scanner and a EC Plan-Neofluar objective with a 20× magnification, 0.50 numerical aperture and M27 thread were used. Images were acquired with the ZEN 3.2 blue edition software and processed and quantified with the Fiji software [63].

2.21. FACS analysis

APs were analyzed or sorted by FACS from the SVF of the adipose tissue using following antibodies: anti-CD140a (PDGFRα)-APC (1:100, 562777, BD Biosciences), anti-LY6A-PECy7 (1:100, 558162, BD Biosciences), anti-CD31-PE (1:100, 553373, BD Biosciences) and anti-CD45-AlexaFluor488 (1:100, 103122, BioLegend), anti-CD45-PE (1:100, 553081, BD Biosciences), anti-CD45-APC-Cy7 (1:100, 561037,

BD Bioscience), anti-CD11b-PerCP, (1:100, 101230, Biolegend) anti-CD11c-APC (1:100, 117310, BioLegend), anti-F4/80-PECy7 (1:100, 25480182, eBioscience) or anti-CD9-AlexaFluor488 (1:100, 11-0091-82, Thermo Fisher Scientific). For Ki67 staining, cells were permeabilized with the Fix/Perm Buffer Set (Biolegend) and incubated with anti-Ki67-FITC (1:2000, 11-5698-82, Thermo Fisher Scientific) for 45 min at 4 °C. FACS was carried out with a BD FACSCanto II (BD Biosciences) and analyzed with the BD FACSDiva Version 6.1.3 software (BD Biosciences). PDGFRα^{+}LY6A^{+}CD31^{-}CD45^{-} cells (APs) were sorted with a BD FACS ARIA apparatus (BD Biosciences) using the BD FACSDIVA v8.0.1 software (BD Biosciences) [36].

2.22. Western blot

Tissues or cultured cells were lysed in lysis buffer containing 1 % SDS, 50 mM Tris pH 7.4, 1 mM sodium orthovanadate, protease cOmplete™ Protease Inhibitor Cocktail inhibitors (Merck) and DNase (benzonase, Sigma). Cell lysates were centrifuged at 16,000*g* for 5 min at 4 °C, supernatants were collected and total protein concentration was measured using Pierce BCA Protein Assay Kit (Thermo Fisher Scientific). 40 µg of protein were loaded onto polyacrylamide gels and proteins were transferred on a nitrocellulose membrane by wet transfer. Membranes were blocked in 5 % non-fat milk or 5 % BSA TBS-T (0.15 M NaCl, 2.7 mM KCl, 24.8 mM Tris-base, 0.1 % Tween-20). Membranes were incubated overnight at 4 °C with an anti-DDK (1:1000, TA50011-100, Origene), anti-eIF5a (1:10,000, 611976, BD Transduction Laboratories™), anti-eIF5a^{Hyp} (1:2000, ABS1064-I-25UL, Sigma-Aldrich), anti-UCP1 (1:1000, ab10983, Abcam), anti-HSL (1:1000, #4107, Cell Signaling), anti-phospho-HSL (1:1000, #4139, Cell Signaling) anti-β-actin (1:1000, #4970, Cell Signaling) or anti-vinculin (1:1000, #4650, Cell Signaling). Membranes were then incubated for 2 h at RT with goat anti-mouse IgG HRP-conjugated (1:3000; Jackson ImmunoResearch) diluted in 5 % non-fat milk in TBS-T. Membranes were revealed using SuperSignal West Pico Chemiluminescent Substrate (Thermo Fisher Scientific) and a luminescent image analyzer, LAS-3000 (Fujifilm). Band intensity was quantified with the Fiji/ImageJ software [63].

2.23. Quantitative RT – PCR

RNA was isolated from frozen tissues with the Trizol Reagent (Thermo Fisher Scientific) after mechanical tissue disruption or from cells with the Nucleospin RNA kit (Macherey-Nagel) according to manufacturer's instructions. RNA isolated with Trizol was subsequently treated with DNase (Thermo Fisher Scientific). Reverse transcription was performed with the iScript cDNA Synthesis kit (Biorad) and cDNA was analyzed by qPCR using the SsoFast Eva Green Supermix (Bio-Rad), a CFX384 real-time System C1000 Thermal Cycler (Bio-Rad) and the Bio-Rad CFX Manager 3.1 software. The relative gene expression was calculated using the ΔΔCt method, *18S* expression was used as a reference gene. Primers used are shown in Table S1.

2.24. Free fatty acid measurement

Fatty acids were quantified in the serum of mice using a fluorometric assay kit (Cayman Chemical) per manufacturer's instructions.

2.25. Triglyceride measurement

TGs were measured in mouse liver tissue using a commercially available kit (Abcam). Briefly, 100 mg of liver tissue were homogenized in 1 ml of 5 % Triton X-100. Then, the samples were heated to 95 °C and cooled to room temperature twice. Thereafter, samples were centrifuged, and the TG content in the supernatant was quantified according to manufacturer's instructions.

2.26. Quantification and statistical analysis

For statistical analysis Mann-Whitney *U* test, Wilcoxon test, Kruskal-Wallis test, or ANCOVA were performed, as indicated in the figure legends. Statistical analysis and data plotting were done with the GraphPrism 10 software. Sample numbers are mentioned in the figure legends, $p < 0.05$ or adjp < 0.05 was set as a significance level.

3. Results

3.1. Polyamine metabolism declines with obesity

We analyzed by bulk RNA-seq the inguinal SAT of C57BL6/J mice fed for 20 weeks a LFD or a HFD. HFD feeding induced body weight gain, glucose intolerance and insulin resistance [36,37] and caused transcriptional remodeling of the adipose tissue (Fig. S1A). Expression of several lipid metabolism-related genes was upregulated in the adipose tissue of HFD mice (Fig. S1B). Furthermore, we observed enrichment of inflammatory response-related changes (Fig. S1C, D) in accordance with the well-documented pro-inflammatory profile of the adipose tissue in obesity [3]. By contrast, mRNAs encoding proteins mediating arginine and proline metabolism were downregulated in the adipose tissue of HFD-fed mice (Figs. 1A–C, S1E); among the downregulated genes were genes related to polyamine metabolism, like *Azin2*, *Odc1* and *Sms*, shown by RNA-seq and qPCR (Fig. 1B–D). Together, our data suggest that diet-induced obesity downregulated gene expression related to polyamine metabolism in the adipose tissue.

Next, we set out to identify cells of the adipose tissue expressing components of polyamine metabolism. ARG1, ODC1 and SAT1 were expressed in PDGFRα^{+} APs in adipose tissue of 8 week-old CD-fed mice, shown by immunofluorescent stainings (Fig. 1E). *Azin2* expression was demonstrated by RNAscope in PDGFRα^{+} APs in SAT and GAT (Figs. 1F, S1F, Movie S1). Of note, *Pdgfra* was expressed in CD45^{-}CD31^{-} cells of the SVF (Fig. S1G) and not in the AF consisting of mature adipocytes (Fig. S1H). Expression of *Azin2*, *Azin1* (the abundant isoform of *Azin2*), *Odc1*, *Srm*, *Sms* and *Sat1* was detected in CD45^{-}CD31^{-} SVF cells and their expression was higher in CD45^{-}CD31^{-} compared to CD45^{+} or CD31^{+} SVF cells (Fig. 1G) [29,30]. *Arg1* expression was similar in CD45^{-}CD31^{-}, CD45^{+} and CD31^{+} SVF cells (data not shown). Although *Azin2* mRNA was detected at relatively low amounts in the white adipose tissue compared to other tissues, such as the brain or the adrenal glands (Fig. S1I), *Azin2* was highly expressed in APs compared to other cell types, such as mature adipocytes, ATMCs and hepatocytes (Fig. S1J). *Odc1*, *Srm*, *Sms*, *Sat1* and *Azin1* were variantly expressed in different adipose tissues and organs (Fig. S1K). Of note, *Azin1* expression was similar in APs (CD45^{-}CD31^{-}) and mature adipocytes (Fig. S1L).

Strikingly, *Azin2* mRNA was diminished in the adipose tissue of mice fed for 20 weeks a HFD compared to young CD-fed mice or mice fed for 20 weeks a control LFD (Fig. 1F). This was associated with a corresponding reduction of AP numbers after the 20-week feedings (Figs. 1F, S1M). Additionally, the expression of *Azin2*, *Arg1*, *Odc1*, *Srm* and *Sms* declined upon in vitro differentiation of mouse APs to adipocytes (Figs. 1H, S1N), even though full adipocyte maturity (characterized by appearance of a single large lipid droplet) was not reached in this in vitro system, in which multilocular adipocytes formed instead (Fig. S4I, J). Similarly, *AZIN2* and *SMS* mRNA expression was also diminished upon differentiation in human preadipocytes (Fig. 1I). Thus, key components of polyamine metabolism, including AZIN2, are expressed in APs and their expression declines with adipocyte differentiation.

3.2. IL4 upregulates Azin2 expression in APs

Next, we set out to investigate whether factors deriving from the adipose tissue microenvironment regulate polyamine metabolism in APs. Given that in the adipose tissue polyamine metabolism is downregulated (Figs. 1A, B, D, F, S1E) and the immune profile radically

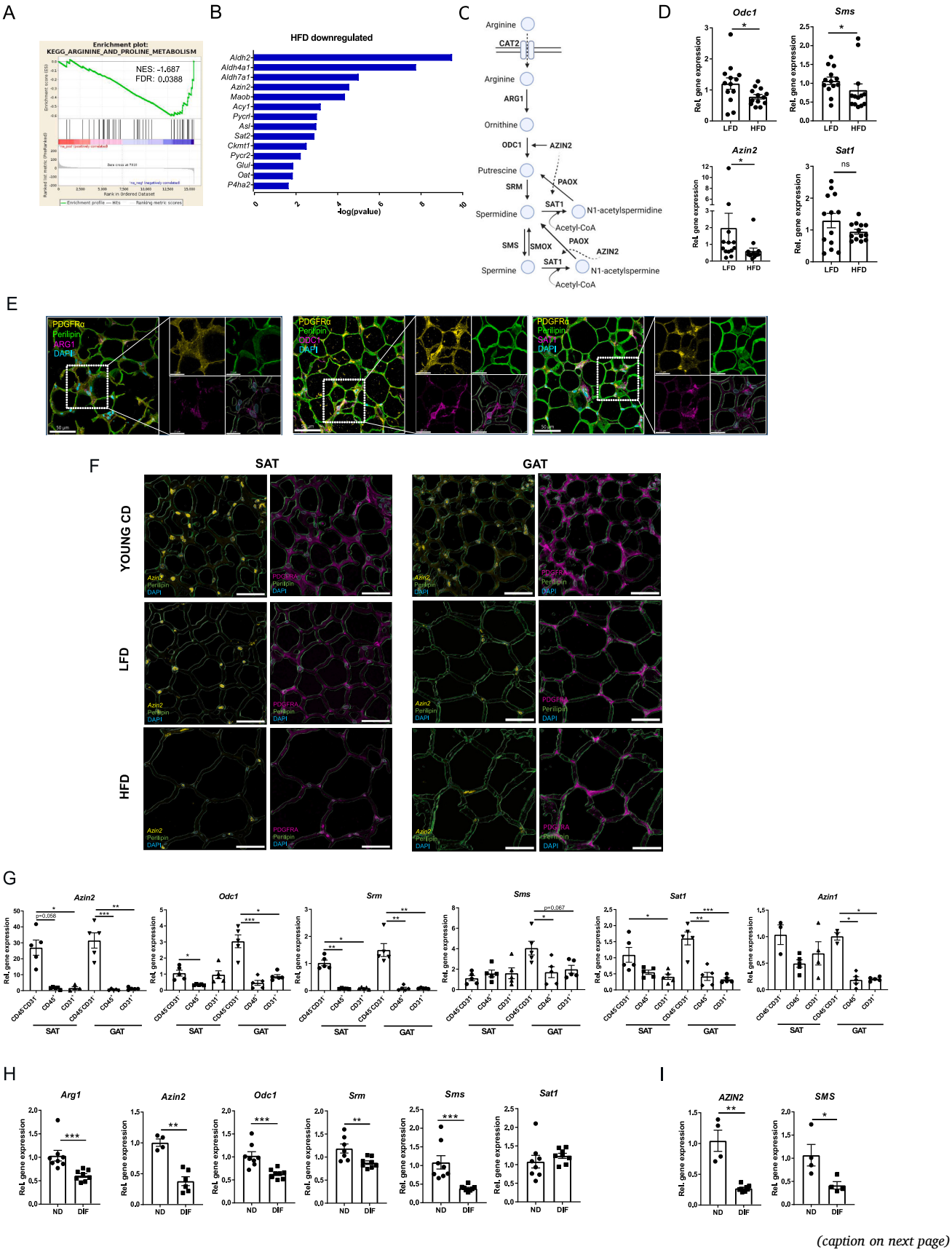

(caption on next page)

Fig. 1. Expression of proteins involved in polyamine metabolism is downregulated in the adipose tissue with obesity.
A–B. Bulk RNA-seq analysis in SAT of mice fed for 20 weeks a HFD or LFD ($n = 4$ mice per group): GSEA analysis for KEGG_arginine and proline metabolism (A) and downregulated arginine and proline metabolism-related genes (B) in SAT of HFD vs LFD mice. C. Schematic presentation of polyamine metabolism. D. *Odc1*, *Sms*, *Azin2* and *Sat1* relative gene expression in SAT of mice fed for 20 weeks a HFD or LFD ($n = 13$ mice per group). E. Immunofluorescence (ARG1 (magenta), ODC1 (magenta) and SAT1 (magenta), PDGFRα (yellow), Perilipin (green)) and DAPI staining in SAT of 8 week-old mice fed a CD. Scale bar, 50 μm. Representative images from SAT of 2 mice are shown. F. RNAScope for *Azin2* and immunofluorescence for PDGFRα and perilipin in SAT and GAT of 8 week-old mice fed a CD and mice fed for 20 weeks a LFD or a HFD. Scale bar, 50 μm. Representative images from 3 parts per tissue of 2 mice are shown. G. *Azin2*, *Odc1*, *Srm*, *Sms*, *Sat1* and *Azin1* expression in $CD45^+$, $CD31^+$ and $CD45^-CD31^-$ SVF populations isolated from SAT and GAT of wt mice ($n = 3$–5 mice). H. *Arg1*, *Azin2*, *Odc1*, *Srm*, *Sms* and *Sat1* expression in differentiated (DIF) or non-differentiated (ND) cultured murine SAT APs (cultures from n = 4–8 mice). I. *AZIN2* and *SMS* expression in differentiated or non-differentiated cultured human preadipocytes (n = 4–8). Gene expression in D, G–I was determined by qPCR using *18S* as a housekeeping gene. Data in D, G–I are shown as mean ± SEM. Mann-Whitney U (D, H, I) or Kruskal-Wallis test (G) tests were used for statistical analysis. $^*p < 0.05$, $^{**}p < 0.01$, $^{***}p < 0.001$, ns: not significant. NES: Normalized enrichment score; FDR: False discovery rate. (For interpretation of the references to color in this figure legend, the reader is referred to the web version of this article.)

changes with obesity (Fig. S1C, D) [3,64], we considered that immune signals may regulate polyamine metabolism in APs. IL4 is a type 2 immunity cytokine, which targets preadipocytes [39]. In adipose tissue, eosinophils, sustained by IL33 and IL5-driven signaling networks, are a major source of IL4 [65,66]. IL4Rα is expressed in SAT APs (Fig. S2A), and its expression is reduced upon adipogenesis (Fig. 2A). Accordingly, *Il4ra* expression is higher in $CD11b^-$ SVF cells than in the AF (Fig. S2B). IL4 induced transcriptional reprograming of cultured non-differentiated APs (sorted as $PDGFR\alpha^+LY6A^+CD31^-CD45^-$ cells) (Fig. 2B). Arginine and proline metabolism was the top among the metabolic pathways with positive enrichment as shown by EGSEA analysis (Fig. 2C) and *Azin2*, *Arg1* and *Srm* were among the upregulated arginine metabolism-related mRNAs (Fig. 2D, E) following IL4 treatment of non-differentiated APs. IL4 also increased the expression of different amino acid transporters of the solute carrier family 7 (SLC7), among which *Slc7a2*, encoding for the arginine transporter CAT2 (cationic amino acid transporter 2) was one of the most strongly upregulated (Fig. 2E, F) [67]. Similarly, IL4 increased *AZIN2* mRNA expression in human preadipocytes (Fig. 2G). The effect of IL4 on *Azin2* expression was abolished by silencing of STAT6, the transcription factor mediating the majority of the effects of IL4 and IL13 (Fig. S2C) [68]. IL13, which exerts its effects through the type II receptor IL4Rα/IL13Rα1 in non-hematopoietic cells [69], also increased *Azin2* expression in mouse APs (Fig. S2D). Moreover, IL4 and IL13 upregulated *Azin2*, *Slc7a2* and *Arg1* expression in adipose tissue explants from wild type (wt) but not $Il4ra^{-/-}$ mice (Fig. 2H).

IL4 was previously reported to inhibit adipogenesis [70,71]. In accordance, wt mice treated with IL4 during the 2 last weeks of a 6-week-long HFD feeding showed reduced body weight gain (Fig. S2E), diminished expression of adipogenic genes, such as *Pparg*, CCAAT/enhancer-binding protein-alpha (*Cebpa*), adiponectin (*Adipoq*), acyl-CoA synthetase long chain family member 1 (*Acsl1*), *Cd36*, lipoprotein lipase (*Lpl*), patatin-like phospholipase domain containing 2 (*Pnpla2*) and lipase, hormone sensitive (*Lipe*) (Fig. S2F) and increased AP numbers per adipose tissue weight (Fig. S2G). As expected, expression of genes encoding for proteins related to type 2 immunity, such as chitinase-like 3 (*Chil3*), C-type lectin domain family 10 (*Clec10a*), and mannose receptor, C type 1 (*Mrc1*), was increased in the SAT SVF of IL4-relative to PBS-treated mice (Fig. S2H) [68]. However, IL4 also increased *Azin2*, *Slc7a2* and *Arg1* expression in the SAT SVF of the mice (Fig. 2I).

Furthermore, infection of mice with *N. brasiliensis*, which causes a potent type 2 immune response and eosinophil accumulation in the adipose tissue [65,72], downregulated *Pparg* and *Cd36* expression (Fig. S2I) and increased *Azin2* and *Srm* expression in GAT (Fig. 2J).

In order to validate these findings in human adipose tissue, we mined the public GEPIA2 database (http://gepia2.cancer-pku.cn/#index) [73] for the expression of type 2 immune mediators in correlation with *AZIN2* expression. Expression of *IL4*, *IL13*, *STAT6*, *IL5* and *IL33* positively correlated with *AZIN2* expression in subcutaneous and visceral adipose tissue (Fig. S2J–R). These data collectively demonstrate that type 2 immunity upregulates *Azin2* expression in APs.

3.3. AZIN2 promotes polyamine acetylation and regulates acetyl-CoA amounts in APs

In order to explore the role of AZIN2, we generated mice with global *Azin2* deletion. *Azin2* expression was abolished in SAT APs of $Azin2^{-/-}$ mice (Fig. S3A). GAT-derived $Azin2^{-/-}$ APs, cultured in a spermidine-free medium, in order to exclude AZIN2-dependent differences in spermidine uptake [74], produced lower spermidine and spermine amounts compared to wt APs (Fig. 3A left panel, 3B), thereby validating that AZIN2 promotes ODC1 function and polyamine production [25]. Strikingly, N1-acetylspermidine amounts were also diminished in GAT $Azin2^{-/-}$ APs (Fig. 3A right panel). Accordingly, N1-acetylspermidine and N1-acetylspermine amounts were also lower in supernatants of $Azin2^{-/-}$ GAT explants compared to supernatants of wt explants (Fig. 3C). Moreover, N1-acetylspermidine amounts were reduced in culture supernatants of differentiated $Azin2^{-/-}$ SAT APs in comparison to wt counterparts (Fig. S3B), suggesting that despite its reduced expression upon differentiation (Fig. 1H), AZIN2 is still required for efficient polyamine acetylation in differentiated APs. Moreover, IL4 increased N1-acetylspermidine amounts in wt but not $Azin2^{-/-}$ SAT APs (Fig. 3D), indicating that IL4 promotes polyamine acetylation in an AZIN2-dependent manner. We also used *Azin2* siRNA silencing as a comparator loss-of-function approach to ensure that $Azin2^{-/-}$ mice-derived APs had not undergone substantial metabolic rewiring in terms of polyamine metabolism (Fig. S3C). *Azin2* mRNA silencing reduced intracellular and exported amounts of N1-acetylspermidine in SAT APs, decreased putrescine amounts and, almost significantly, increased ornithine levels (Fig. 3E, F), confirming the effect of AZIN2 on promoting ODC1-mediated conversion of ornithine to putrescine [25,30,75].

Spermidine and spermine acetylation requires acetyl-CoA (Fig. 1C) [20]. Given that AZIN2 promotes polyamine acetylation (Fig. 3A, C, E, F), we tested if AZIN2 regulates acetyl-CoA amounts in APs. Total acetyl-CoA amounts were strikingly increased in both undifferentiated and differentiated $Azin2^{-/-}$ APs compared to wt controls (Figs. 3G, S3D). In contrast, *Azin2* cDNA overexpression through plasmid transfection (Fig. S3E) reduced acetyl-CoA in 3T3-L1 preadipocytes compared to pCMV-transfected cells (Fig. 3H). These findings collectively suggest that AZIN2 promotes polyamine acetylation and is therefore a key regulator of acetyl-CoA amounts in APs.

Moreover, incubation of APs with spermidine fueled N1-acetylspermidine production (Fig. 3I) and diminished acetyl-CoA amounts (Fig. 3J, left panel). Similarly, putrescine and spermine also diminished acetyl-CoA levels in APs (Fig. 3J, middle and right panels), indicating that polyamine acetylation is driven by substrate availability and associates with reduction in acetyl-CoA amounts.

Spermidine serves as a substrate for the hypusination of a conserved lysine residue in eukaryotic initiation factor 5A (eIF5A). Hypusinated eIF5A ($eIF5A^{Hyp}$) promotes the expression of mitochondrial proteins involved in oxidative phosphorylation and increases fatty acid oxidation [76,77]. Moreover, $eIF5A^{Hyp}$ is a key regulator of macrophage responses in the adipose tissue [27,78]. However, its role in APs remains unknown.

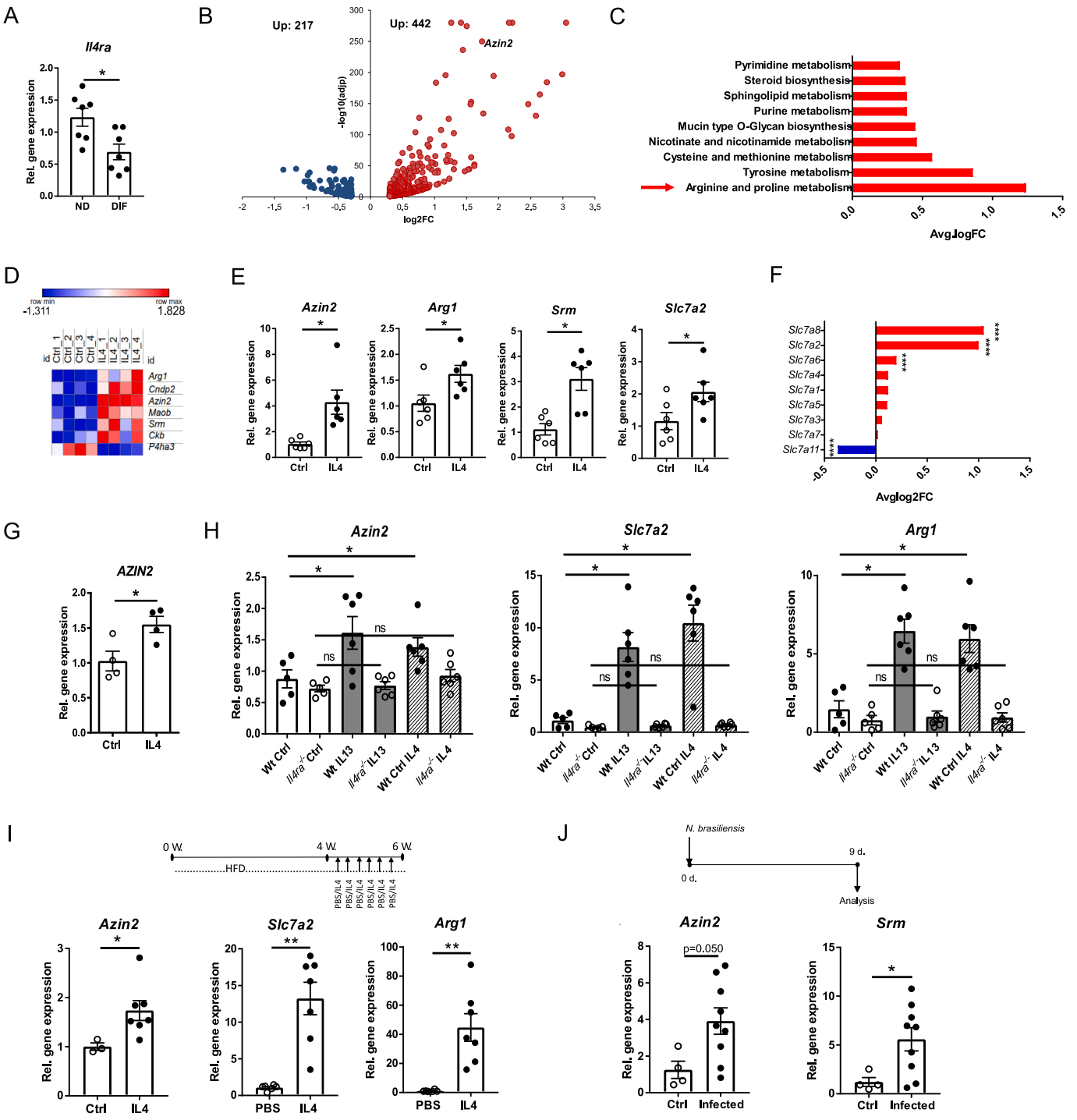

Fig. 2. IL4 upregulates *Azin2* expression in APs.

A. *Il4ra* expression in differentiated and non-differentiated SAT APs assessed by qPCR (cultures from $n = 7$ mice). B–D, F. Bulk RNA-seq was performed in mouse SAT APs treated for 4 h with IL4 (20 ng/ml) or not (cultures from $n = 4$ mice). Volcano plot for differentially expressed genes (DEG) with padj<0.05 log2FC > 0.3 and <−0.3 (B), positively enriched KEGG metabolic pathways based on EGSEA analysis (C), heatmap for arginine metabolism genes (D) and expression of Slc family 7 cationic amino acid transporters (F) in IL4-treated vs control APs. E. *Azin2*, *Arg1*, *Srm* and *Slc7a2* expression in mouse APs treated for 4 h with IL4 (20 ng/ml) or not (Ctrl) (cultures from $n = 6$ mice). G. *AZIN2* expression in human preadipocytes treated for 24 h with IL4 (12 ng/ml) or not (Ctrl) (n = 4). H. *Azin2*, *Slc7a2* and *Arg1* expression in GAT explants from *Il4ra*$^{-/-}$ and wt mice treated for 4 days with 50 ng/ml IL4 or IL13 or not ($n = 5$–6 mice per genotype). I. *Azin2* expression in SAT SVF, and *Slc7a2* and *Arg1* in SAT of mice fed for 6 weeks a HFD and treated every 2 days with PBS or IL4 + a-IL4 during the last 2 feeding weeks, as depicted in the scheme (n = 3–7 mice per group). J. *Azin2* and *Srm* expression in GAT of mice infected with *N. brasiliensis* or control mice 9 days post-infection ($n = 4$–9 mice per group). Gene expression in A, E, G–J was determined by qPCR using *18S* as a housekeeping gene and shown as mean ± SEM. For statistical analysis Mann-Whitney *U* test was used in A, G, I, J; Wilcoxon test in E and Kruskal-Wallis test was used in H, *$p < 0.05$, **$p < 0.01$, ****$p < 0.0001$, ns: not significant.

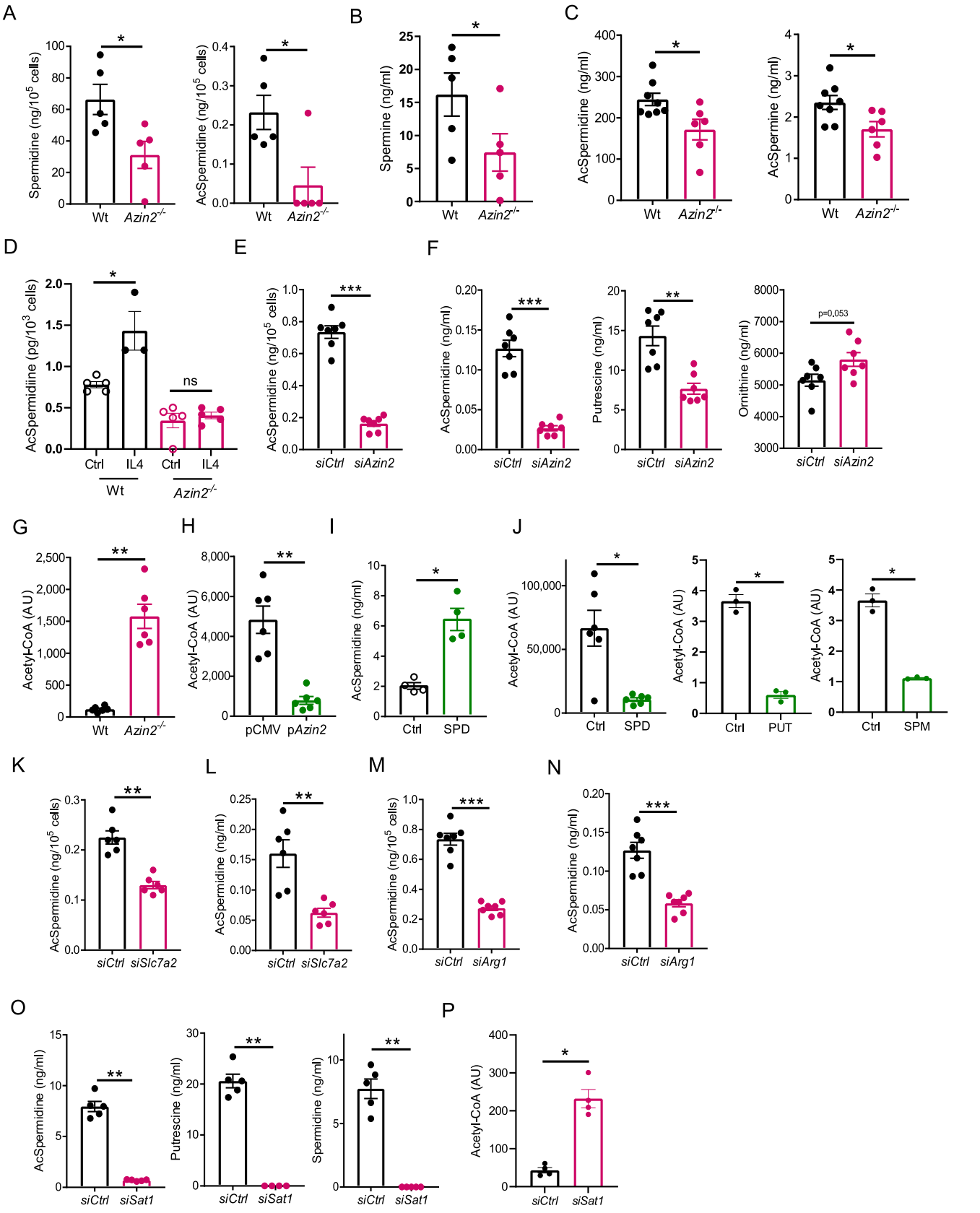

(caption on next page)

Fig. 3. AZIN2 promotes polyamine acetylation and negatively regulates acetyl-CoA in APs.
A. Intracellular spermidine and N1-acetylspermidine levels in undifferentiated cultured wt and *Azin2*$^{-/-}$ GAT APs (cultures from n = 5 mice per group). B. Spermine concentration in the cell culture supernatant of in vitro cultured wt and *Azin2*$^{-/-}$ GAT APs (cultures from n = 5 mice per group). C. N1-acetylspermidine and N1-acetylspermine concentrations in supernatants of GAT explants from wt and *Azin2*$^{-/-}$ mice kept 18 h in culture (cultures from n = 6–8 mice per group). D. N1-acetylspermidine concentration in cell lysates of wt and *Azin2*$^{-/-}$ SAT APs treated for 24 h with IL4 (20 ng/ml) (cultures from n = 3–5 mice per genotype). E, F. SAT APs were transfected 3 times over one week of differentiation with si*Azin2* or siCtrl and N1-acetylspermidine, putrescine and ornithine were measured in the cell lysates (E) and cell culture supernatants (F) (cultures from n = 7 mice). G. Relative abundance of acetyl-CoA in non-differentiated wt and *Azin2*$^{-/-}$ SAT APs shown as peak intensity assessed by LC-MS/MS (cultures from n = 6 mice per group). H. Relative abundance of acetyl-CoA levels in 3T3-L1 preadipocytes transfected with an *Azin2* overexpressing plasmid or a control plasmid (pCMV) shown as peak intensity assessed by LC-MS/MS (n = 6 biological replicates). I. N1-acetylspermidine concentration in cell culture supernatants in SAT APs treated with spermidine (SPD, 10 μM) during 1 week of differentiation (cultures from n = 4 mice). J. Relative abundance of acetyl-CoA in SAT APs treated for 24 h with spermidine (SPD, 10 μM), putrescine (PUT, 10 μM) or spermine (SPM, 10 μM) (cultures from n = 3–6 mice). Note: the Ctrl samples in the middle and right panel are the same. K, L. N1-acetylspermidine concentrations in cell lysates (K) and cell culture supernatants (L) of undifferentiated SAT APs transfected with si*Slc7a2* or siCtrl (cultures from n = 6 mice). M, N. N1-acetylspermidine concentrations in cell lysates (M) and cell culture supernatants (N) of SAT APs transfected 3 times over one week of differentiation with si*Arg1* or siCtrl (cultures from n = 7 mice). O. N1-acetylspermidine, putrescine and spermidine concentrations in cell culture supernatants of undifferentiated SAT APs transfected with si*Sat1* or siCtrl (cultures from n = 5 mice). P. Relative abundance of acetyl-CoA in non-differentiated APs transfected with si*Sat1* or siCtrl (cultures from n = 4 mice). Data are shown as mean ± SEM. Mann-Whitney U test was used for statistical analysis. *$p < 0.05$, **$p < 0.01$, ***$p < 0.001$, ns: not significant. AU: Arbitrary units. Data of 'siCtrl' samples are the same in E and M, and F left and N.

Here, we examined the effect of AZIN2 deficiency on eIF5A hypusination in APs and whole adipose tissue. However, AZIN2 deficiency did not alter total eIF5A or eIF5A^{Hyp} levels neither in cultured SAT APs nor in whole SAT (Fig. S3F, G). These observations indicate that the effects of AZIN2 deficiency in APs are eIF5A^{Hyp}-independent suggesting context- and cell type-dependent regulation of eIF5A hypusination.

Next, we examined whether polyamine acetylation depends on arginine uptake and de novo arginine-dependent polyamine synthesis. *Slc7a2* silencing (Fig. S3H) reduced N1-acetylspermidine levels in SAT AP cell lysates and cell culture supernatants (Fig. 3K, L). Similarly, *Arg1* silencing (Fig. S3I) also reduced intracellular and exported N1-acetylspermidine levels in SAT APs (Fig. 3M, N) suggesting that production of acetylated polyamines requires CAT2-dependent uptake of arginine and its conversion to ornithine and polyamines. However, *Slc7a2* and *Arg1* silencing did not completely abolish N1-acetylspermidine production (Fig. 3K–N) indicating that ornithine may additionally derive from sources other than arginine, like glutamine or proline [27,79]. In fact, APs express Δ1-pyrroline-5-carboxylate (P5C) synthase (P5CS, aldehyde dehydrogenase *Aldh18a1*), P5C reductase (P5CR, Pyrroline-5-carboxylate reductase 1 and 2, *Pycr1*, *Pycr2*) and ornithine aminotransferase (*Oat*), which mediate glutamine and proline metabolism to ornithine (data not shown) [27]. Hence, glutamine and proline may also fuel polyamine metabolism in APs.

Finally, *Sat1* silencing (Fig. S3J) blunted not only N1-acetylspermidine production but also putrescine and spermidine levels (Fig. 3O), standing in accordance with putrescine regeneration from N1-acetylspermidine through the polyamine flux (Fig. 1C) [20]. Furthermore, similarly to AZIN2 knockdown, *Sat1* silencing strongly increased acetyl-CoA amounts in APs (Fig. 3P).

3.4. AZIN2 inhibits de novo adipogenesis via regulation of histone acetylation

Acetyl-CoA is required for histone acetylation, a central mechanism of epigenetic regulation [80]. As we found that AZIN2 downregulates acetyl-CoA levels in APs (Figs. 3G–H, S3D), we hypothesized that AZIN2 may indirectly affect histone acetylation in APs. H3K27ac demarks activated enhancers of key adipogenic genes [18,81,82]. Hence, we performed ChIP-seq analysis for H3K27ac in differentiated *Azin2*$^{-/-}$ and wt SAT APs and identified 10,953 sites of H3K27ac enrichment in *Azin2*$^{-/-}$ compared to wt APs (Fig. 4A). These sites were detected in distal intergenic regions, promoter regions (2–3, 1–2 and <1 kb), regions encoding for 5′ and 3′ UTR, exons and introns (Figs. 4A, S4A). In wt APs 4121 sites were H3K27ac enriched compared to *Azin2*$^{-/-}$ APs (Fig. S4A). Accordingly, the genome-wide H3K27ac distribution of the ChIP-seq peaks across transcriptional start sites (TSS) (±5 kb) and in gene regions between TSS and transcription end sites (TES) was higher in *Azin2*$^{-/-}$ compared to wt APs (Figs. 4B and S4B, respectively). Many sites with increased H3K27ac amounts in *Azin2*$^{-/-}$ APs were associated with genes encoding proteins linked to lipid metabolism, negative regulation of cell cycle, hypoxia and senescence (Fig. 4C). A number of genes related to lipid metabolism showed greater H3K27ac enrichment in their promoter regions, exons, introns, regions encoding for 5' UTR and distal intergenic regions in *Azin2*$^{-/-}$ compared to wt APs, such as *Pparg*, *Cebpa*, *Cebpd*, *Cebpe*, perilipin 4 (*Plin4*), stearoyl-coenzyme A desaturase 2 (*Scd2*), *Scd4*, acetyl-Coenzyme A acetyltransferase 2 (*Acat2*), acetyl-Coenzyme A carboxylase alpha (*Acaca*), ceramide synthase 3 (*Cers3*), lipid droplet associated hydrolase (*Ldah*), adiponectin receptor 2 (*Adipor2*), glycerol-3-phosphate acyltransferase 3 (*Gpat3*), peroxisome proliferative activated receptor, gamma, coactivator 1 alpha (*Ppargc1a*) and fatty acyl CoA reductase 1 (*Far1*) (Fig. S4C–G).

Adipogenesis is initiated with increased expression of C/EBPβ and C/EBPδ, which subsequently cooperate to induce the expression of PPARγ and C/EBPα; the latter activate the transcription of a wide range of factors required for adipocyte maturation [18]. H3K27ac enrichment of *Pparg* and *Cebpa* gene enhancers indicates their activation and coincides with adipogenic differentiation [18,81–83]. In the *Azin2*$^{-/-}$ APs we found enhanced H3K27ac enrichment in the 5' UTR and intron 2 of the *Pparg2* gene and the *Cebpa* enhancer (distal intergenic region) (*Cebpa* + 25.7 kb) (Figs. 4D, S4D, F, G). The 5′ UTR of the *Pparg2* gene (starting 60 kb downstream of the *Pparg1* TSS) acts as an enhancer of *Pparg1* during initiation of differentiation and then promotes expression of *Pparg2* encoding for *Pparg* mRNA [81]. We verified by ChIP-qPCR increased H3K27ac presence in the *Pparg2* promoter in differentiated *Azin2*$^{-/-}$ compared to wt APs, using primers binding 251–144 bp upstream of the *Pparg2* TSS (Fig. 4E). Moreover, H3K9 acetylation was also reported to increase in the *Pparg2* promoter during adipogenesis [84]. Increased H3K9ac enrichment was indeed detected in the *Pparg2* promoter region (251–144 bp upstream of the *Pparg2* TSS) in differentiated *Azin2*$^{-/-}$ compared to wt APs (Fig. 4F). Accordingly, *Pparg* and *Cebpa* expression was elevated in *Azin2*$^{-/-}$ SAT APs (Figs. 4G, S4H). These findings suggest that AZIN2 reduces H3K27ac marks in key adipogenic genes, thereby downregulating their expression.

Next, we examined the adipogenic potential of *Azin2*$^{-/-}$ APs. Lipid accumulation was significantly increased in in vitro differentiated *Azin2*$^{-/-}$ compared to wt SAT APs (Figs. 4H, I, S4I). *Slc7a2* or *Arg1* siRNA silencing also increased SAT AP adipogenic differentiation (Figs. S4J, S3H, I). Accordingly, *Arg1*, *Sat1* and *Odc1* mRNA silencing upregulated *Pparg* expression (Figs. 4K, S3I–K). These findings indicate that AP differentiation is regulated by arginine uptake, polyamine synthesis and polyamine acetylation. We next tested whether supply of substrates would reduce AP adipogenic differentiation. Consistent with reducing acetyl-CoA amounts (Fig. 3J), spermidine suppressed AP differentiation and the expression of adipogenic mediators (*Pparg*, *Cebpa*,

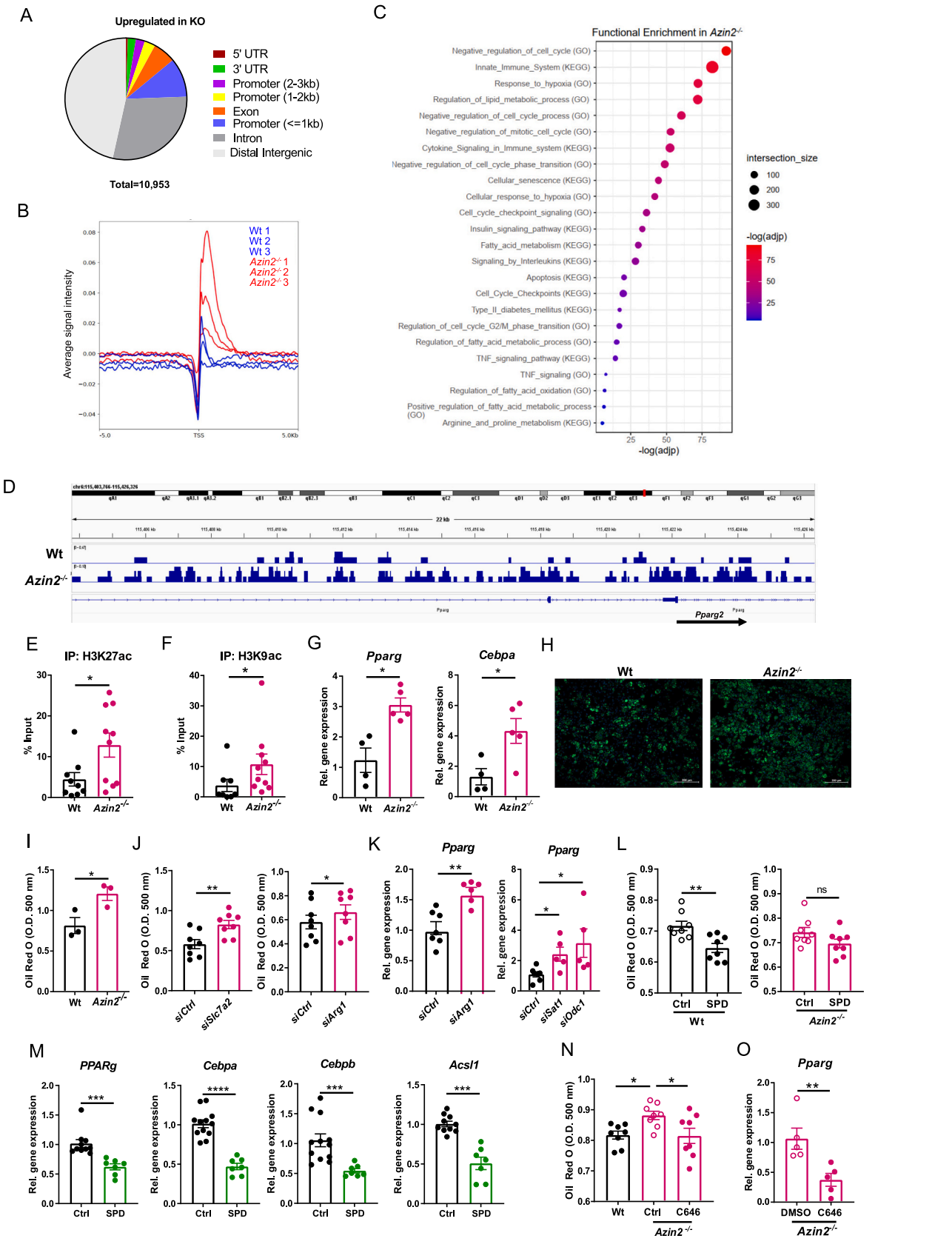

(caption on next page)

Fig. 4. AZIN2 inhibits adipogenesis through regulation of histone acetylation.
A-D. Bulk ChIP-Seq was performed after IP for H3K27ac in in vitro differentiated wt and *Azin2*$^{-/-}$ SAT APs (APs from 2 mice were pooled in one sample, n = 3 samples per group): Global DNA distribution of H3K27ac marks upregulated in *Azin2*$^{-/-}$ SAT APs (A). Histogram of the H3K27ac signal intensity in wt and *Azin2*$^{-/-}$ SAT APs (B). Enriched GO terms and pathways and KEGG pathways in *Azin2*$^{-/-}$ compared to wt SAT APs plotted for the –log(adjp) value based on genes with enhanced H3K27ac signal in *Azin2*$^{-/-}$ versus wt APs (C). Integrative Genomic Viewer (IGV) screenshots showing H3K27ac marks in the −16 kb region upstream of the *Pparg2* TSS in representative wt and *Azin2*$^{-/-}$ SAT AP samples (D). E, F. Abundance of H3K27ac (E) and H3K9ac (F) 251–144 bp upstream of the *Pparg2* TSS in differentiated wt and *Azin2*$^{-/-}$ SAT APs assessed by ChIP-qPCR and shown as % of input (cultures from *n* = 8–10 mice per group). G. *Pparg* and *Cebpa* expression in differentiated wt and *Azin2*$^{-/-}$ SAT APs (cultures from n = 4–5 mice per group). H. Representative images of in vitro differentiated wt and *Azin2*$^{-/-}$ SAT APs stained with BODIPY. Scale bar, 200 μm (a representative image of cultures from 1 out of 8 mice per group is shown). I. Quantification of Oil Red O staining of in vitro differentiated wt and *Azin2*$^{-/-}$ SAT APs (cultures from n = 3 mice per group). J. Quantification of Oil Red O staining in SAT APs transfected 3 times during one week of differentiation with siRNA against *Slc7a2* or *Arg1* or non-targeting control siRNA (siCtrl) (cultures from n = 8 mice, siCtrl samples in the left and right panel are the same). K. *Pparg* expression in SAT APs transfected 3 times during one week of differentiation with siRNA against *Arg1*, *Sat1*, *Odc1* or non-targeting siRNA (siCtrl) (cultures from n = 5–7 mice). L. Quantification of Oil Red O staining in wt and *Azin2*$^{-/-}$ SAT APs treated or not with spermidine (SPD, 10 μM) during in vitro differentiation (cultures from n = 8 mice per genotype). M. *Pparg*, *Cebpa*, *Cebpb* and *Acsl1* expression in differentiated SAT APs treated or not during differentiation with 10 μM spermidine (cultures from n = 7–12 mice). N. Quantification of Oil Red O staining in wt and *Azin2*$^{-/-}$ SAT APs treated with C646 (4 μM) or equal amount of DMSO (Ctrl) during in vitro differentiation (cultures from n = 8 mice per genotype). O. *Pparg* expression in *Azin2*$^{-/-}$ SAT APs treated with C646 (4 μM) or DMSO during differentiation (cultures from n = 5 mice). Gene expression in G, K, M and O was determined by qPCR using *18S* as a housekeeping gene. All data are shown as mean ± SEM. Mann-Whitney U (E–G, I, K left, L, M, O), Wilcoxon test (J) and Kruskal-Wallis test (K right, N) tests were used for statistical analysis. *p < 0.05, **p < 0.01, ***p < 0.001, ****p < 0.0001; ns: not significant. (For interpretation of the references to color in this figure legend, the reader is referred to the web version of this article.)

Cebpb, *Acsl1*) in wt but not *Azin2*$^{-/-}$ APs (Figs. 4L, M, S4I), in accordance with the requirement of AZIN2 for spermidine acetylation (Figs. 3A, C, E, F, S3B). Finally, H3 acetylation is catalyzed by the lysine acetyltransferase (KAT) p300/CBP (KAT3A/3B) [83]. Inhibition of p300 by C646 repressed adipogenesis and *Pparg* expression in *Azin2*$^{-/-}$ APs (Fig. 4N, O). Collectively, these findings suggest that AZIN2-driven polyamine metabolism represses adipogenesis through modulating acetyl-CoA levels and downregulation of p300-mediated histone acetylation in regulatory elements of key adipogenic genes.

3.5. AZIN2 deficiency leads to increased adipogenesis in vivo

Next, we examined the in vivo effects of AZIN2 deficiency in the adipose tissue. Eight week-old CD-fed *Azin2*$^{-/-}$ mice had no difference in SAT, GAT, axillary adipose tissue, mesenteric adipose tissue and liver or glucose and insulin tolerance compared to littermate wt mice (Figs. 5A, S5A–F). However, SAT and GAT of *Azin2*$^{-/-}$ mice contained more small adipocytes compared to wt mice (Figs. 5B, S5G). Moreover, the number of total and proliferating (Ki67^{+}) APs per SAT mass was reduced in *Azin2*$^{-/-}$ compared to wt mice (Fig. 5C, D), in accordance with H3K27ac enrichment in genes linked to negative regulation of cell cycle in *Azin2*$^{-/-}$ SAT APs (Fig. 4C).

In order to determine adipogenesis in vivo, bromodeoxyuridine (BrdU) pulse-chase experiments were performed, as depicted in Fig. 5E, based on the fact that proliferating APs at the start of HFD feeding give rise to mature adipocytes during the course of HFD [6]. Mice were fed for 1 week with BrdU through the drinking water and for 8 weeks with HFD, and SAT was immunostained for BrdU, PDGFRa and perilipin (Fig. 5F, left panel). Strikingly, the percentage of BrdU^{+} adipocytes (PDGFRa^{-}) was increased in the SAT of *Azin2*$^{-/-}$ mice (Fig. 5F, right panel), suggesting that APs more efficiently differentiated to mature adipocyte in *Azin2*$^{-/-}$ compared to wt mice. The fact that the amount of APs in SAT was already reduced in lean (CD-fed) *Azin2*$^{-/-}$ mice (Fig. 5C, D), further substantiates that AZIN2 deficiency enhances adipogenesis (Fig. 5F). These data raised the question, whether shrinkage of the AP pool in the lean state is linked to impairments in the adipose tissue upon diet-induced obesity.

3.6. AZIN2 deficiency leads to increased obesity and adipose tissue dysfunction

We next set out to explore the role of AZIN2 in diet-induced obesity (Fig. 6A). *Azin2*$^{-/-}$ HFD-fed mice gained more body weight and demonstrated reduced insulin sensitivity, energy expenditure and oxygen consumption compared to wt littermate mice (Fig. 6B–E) without presenting differences in food intake or locomotion (Fig. S6A, B). In accordance, *Azin2*$^{-/-}$ HFD mice showed increased fat/lean ratio (Fig. 6F) and bigger SAT (Fig. 6G), which contained larger adipocytes compared to wt mice (Fig. 6H). Notably, the acetyl-CoA concentration in SAT was elevated in *Azin2*$^{-/-}$ HFD mice compared to control mice (Fig. 6I), consistent with increased acetyl-CoA amounts in *Azin2*$^{-/-}$ SAT APs (Figs. 3G, S3D). Similar to SAT, GAT was also hypertrophic and contained higher acetyl-CoA amounts in *Azin2*$^{-/-}$ compared to wt HFD mice (Fig. S6C–F).

To further characterize the changes caused by *Azin2* deficiency in fat, we performed bulk RNA-seq in total SAT and GAT of wt and *Azin2*$^{-/-}$ HFD mice. In *Azin2*$^{-/-}$ HFD mice, pathway analysis showed relative upregulation of pathways linked to fat metabolism, PPAR signaling and inflammatory pathways (Fig. 6J) and enrichment of genes related to lipid storage and fatty-acyl-CoA biosynthesis in SAT (Fig. 6K). GAT in *Azin2*$^{-/-}$ HFD mice displayed a pronounced inflammatory profile compared to wt counterparts (Fig. S6G–M). Expression of many genes involved in inflammation, such as Toll-like receptor 8 (*Tlr8*), *Tlr1*, Fc receptor, IgG, low affinity I (*Fcgr1*), *Fcgr4*, *Clec12a*, complement component 3a receptor 1 (*C3ar1*), *Cd68*, S100 calcium binding protein A8 (*S100a8*), integrin alpha D (*Itgad*), *Itgax*, leukocyte immunoglobulin-like receptor, subfamily B, member 4A (*Lilrb4a*), triggering receptor expressed on myeloid cells 2 (*Trem2*), secreted phosphoprotein 1 (*Spp1*), serum amyloid A 3 (*Saa3*), C—C motif chemokine receptor 3 (*Ccr3*), C—C motif chemokine ligand 3 (*Ccl3*) and regulator of G-protein signaling 1 (*Rgs1*) was increased in GAT of *Azin2*$^{-/-}$ compared to wt HFD mice (Fig. S6G). Gene expression related to inflammatory pathways, such as cell adhesion molecules, Toll-like receptor pathway or phagocytosis and *Il6* were upregulated in GAT of *Azin2*$^{-/-}$ HFD-fed mice (Fig. S6H–J) [3,64]. Moreover, expression of *Ccl2*, a key mediator of monocyte recruitment in the adipose tissue, was upregulated and the number of CD11c^{+} and total adipose tissue macrophages was increased, suggesting enhanced monocyte/macrophage recruitment in GAT of *Azin2*$^{-/-}$ HFD-fed mice (Fig. S6K–M) [64].

Increased inflammation was accompanied by changes in the metabolic profile of GAT in *Azin2*$^{-/-}$ HFD mice. Gene expression related to oxidative phosphorylation, citrate cycle, pyruvate metabolism and fatty acid degradation was downregulated, while glycolysis and fructose/mannose metabolism-related gene expression was upregulated in GAT of *Azin2*$^{-/-}$ HFD mice (Fig. S6N, O). In obesity, chronic inflammation in adipose tissue associates with development of fibrosis [4,85]. GAT of *Azin2*$^{-/-}$ mice showed enhanced expression of a number of fibrotic genes, like matrix metallopeptidase 12 (*Mmp12*), *Mmp13*, collagen, type I, alpha 1 (*Col1a1*), *Col3a1*, *Col8a1* and *Cd9* (Fig. S6G, P). Accordingly, the percentage (%) of pro-fibrotic CD9^{high} APs in GAT was increased in *Azin2*$^{-/-}$ compared to wt HFD mice (Fig. S6Q) [86]. These data demonstrate that AZIN2 deficiency promotes adipose tissue

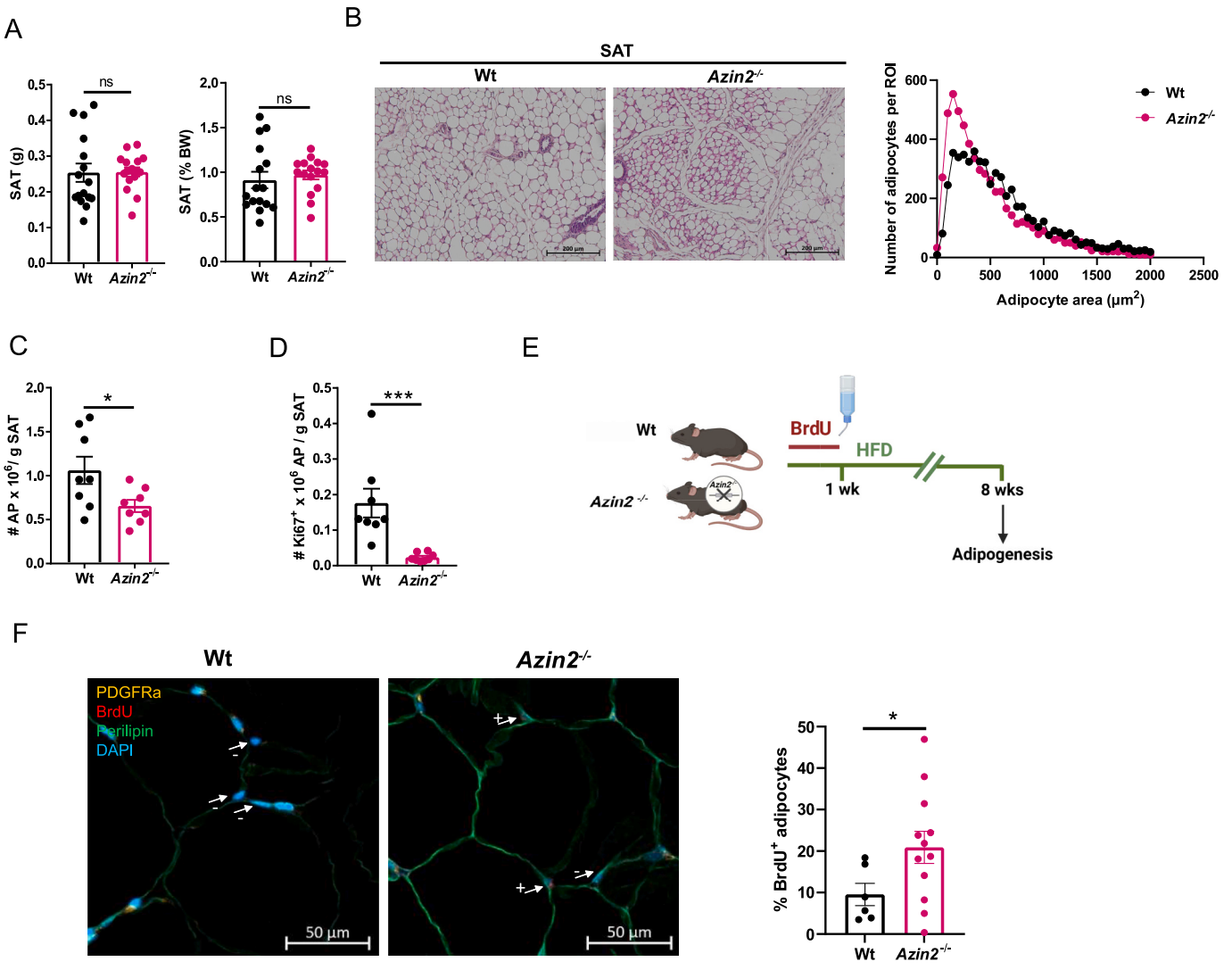

Fig. 5. AZIN2 deficiency leads to increased adipogenesis in vivo.
A–D. Analysis in 8-week old male *Azin2*$^{-/-}$ and wt mice fed a CD. SAT weight net (left panel) or as % of the body weight (right panel) ($n = 16$ mice per group) (A), representative H&E images of SAT (left panel) and frequency distribution of adipocyte size (right panel) (adipocyte size was quantified in 7–10 images per mouse in 2–3 mice/group), scale bar: 200 µm (B), number of total SAT APs (PDGFRα$^+$LY6A$^+$CD31$^-$CD45$^-$) (C) and Ki67$^+$ SAT APs (D) analyzed by FACS (n = 8 mice per group). E. Experimental setup of BrdU pulse-chase experiments in wt and *Azin2*$^{-/-}$ mice. F. Left panel: Immunofluorescence (BrdU (red), PDGFRA (orange), perilipin (green)) and DAPI staining in SAT of wt and *Azin2*$^{-/-}$ mice, representative images are shown. Arrows depict adipocyte nuclei (of PDGFRa$^-$ cells): '+' for BrdU$^+$ or '-'for BrdU$^-$ cells. Scale bar, 50 µm. Right panel: Percentage of BrdU$^+$ adipocyte nuclei out of total adipocyte nuclei was quantified in 2–3 anatomically distanced pieces of SAT deriving from 3 to 4 mice per group. Data are shown as mean ± SEM. Mann-Whitney *U* test was used for statistical analysis. *p < 0.05, ***p < 0.001, ns: not significant. (For interpretation of the references to color in this figure legend, the reader is referred to the web version of this article.)

inflammation, which is in general associated with fibrosis and impaired adipose tissue plasticity [4,85].

Next, we analyzed the lipidomic profile of the adipose tissue of *Azin2*$^{-/-}$ HFD mice, as previously described [43,87]. We found that the total TG acyl chain length was increased and the degree of unsaturation was decreased in SAT of *Azin2*$^{-/-}$ mice (Figs. 6L, S6R). We previously demonstrated that TG in the adipose tissue get overall longer and more unsaturated with obesity [87]. Here we show that AZIN2 deficiency impairs this vital adaptation of the adipocyte TG profile. Moreover, the amount of total DG was increased in SAT of *Azin2*$^{-/-}$ compared to wt HFD mice (Fig. 6M). Similarly to TG, DG species that were upregulated in SAT of *Azin2*$^{-/-}$ mice, had a low degree of unsaturation, i.e. contained 0–2 double bonds (Fig. S6S). Of note, DG inhibit insulin signaling and increased DG content in adipose tissue, muscle and liver associates with insulin resistance [88,89]. In addition, several ceramide species were more abundant in the SAT of *Azin2*$^{-/-}$ compared to wt HFD mice (Fig. 6N). The ceramide content in adipose tissue is increased in obesity and type 2 diabetes, and inhibition of ceramide synthesis in adipocytes reduces inflammation and improves insulin sensitivity [88,90,91]. Notably, the amount of C18:0 ceramide, which was reported to increase with obesity in adipose tissue of human subjects [91,92], was increased in SAT of *Azin2*$^{-/-}$ HFD mice (Fig. 6N). In sum, increased ceramide and DG content and decreased TG unsaturation overall demonstrated disturbed lipid storage in the adipose tissue of *Azin2*$^{-/-}$ mice.

Polyamines promote adipocyte lipolysis upon their release from endothelial cells [32]. Hence, we asked whether AZIN2 deficiency may affect adipose tissue lipolysis. Nevertheless, protein levels of phosphorylated and total hormone sensitive lipase (HSL), adipose triglyceride lipase (*Atgl*) expression or serum free fatty acid (FFA) levels were unaltered in *Azin2*$^{-/-}$ compared to wt control mice (Fig. S7A–C). These data suggest that AZIN2 deficiency does not affect adipocyte lipolysis. This could be explained by the low *Azin2* expression in endothelial cells (Fig. 1G) and indicates that the effects of polyamines may be cell source-dependent [32].

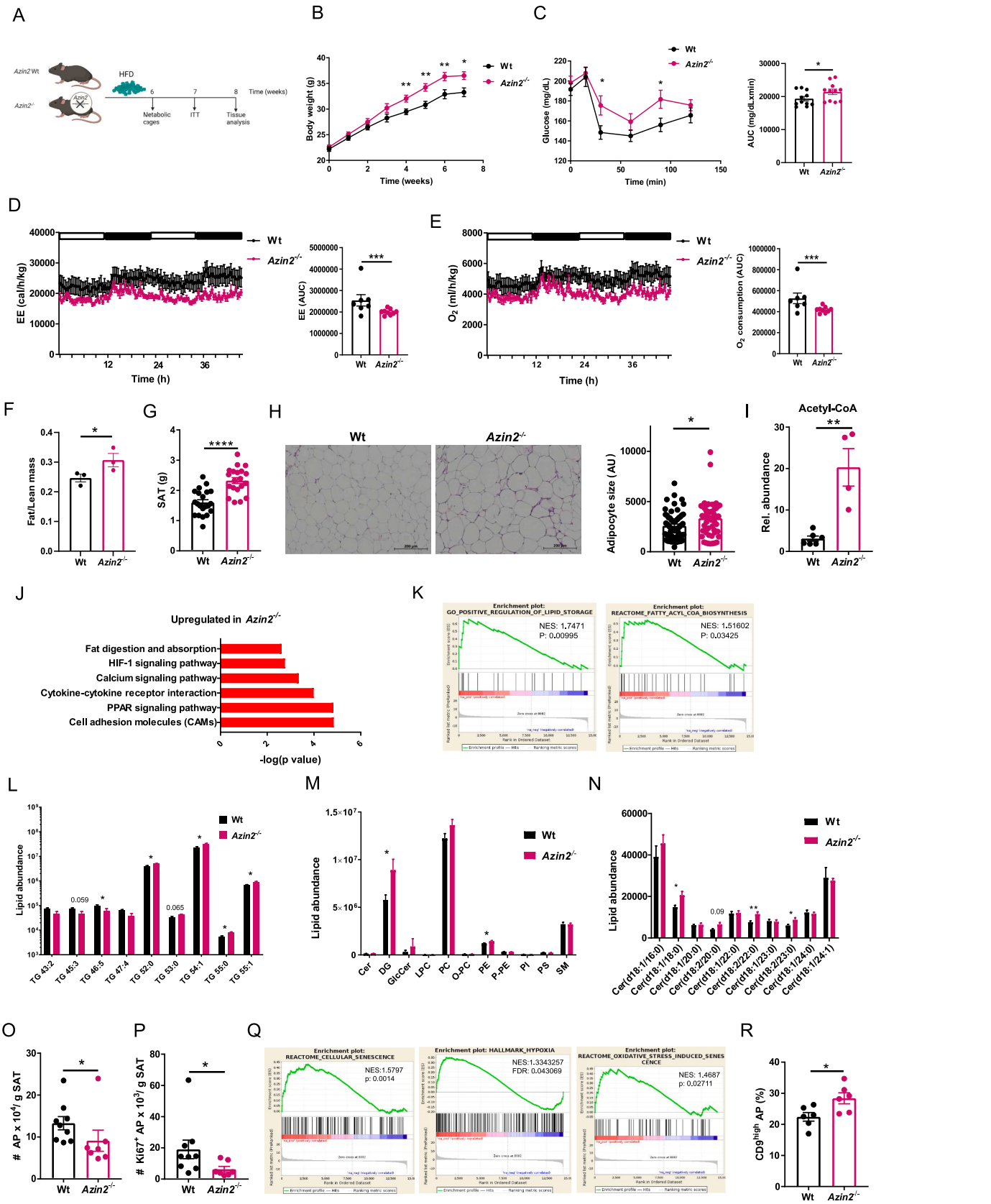

Fig. 6. AZIN2 deficiency leads to increased obesity.

A. Experimental setup. B. Body weight gain in wt and *Azin2*$^{-/-}$ mice fed for 8 weeks a HFD ($n = 15$ mice per group). C. ITT performed at 7 weeks of HFD feeding in wt and *Azin2*$^{-/-}$ mice ($n = 11$ mice per group). Left panel: Blood glucose concentration over time; right panel: area under the curve (AUC). D, E. Energy expenditure (EE) (D) and O_2 consumption (E) measured in metabolic cages in wt and *Azin2*$^{-/-}$ mice fed for 6 weeks a HFD (n = 7–9 mice per group). F. Fat/lean ratio in wt and *Azin2*$^{-/-}$ mice fed for 8 weeks a HFD (n = 3 mice per group). G. SAT weight of wt and *Azin2*$^{-/-}$ mice fed for 8 weeks a HFD (n = 20–21 mice per group). H.

Representative images of H&E staining of SAT from wt and *Azin2*$^{-/-}$ mice fed for 8 weeks a HFD (an image is shown from one out of 10–11 mice), scale bar: 200 μm. Adipocyte size quantification in SAT of wt and *Azin2*$^{-/-}$ mice fed for 8 weeks a HFD (adipocyte size was quantified in 9–10 sections per mouse in 6 mice/group). I. Relative abundance of acetyl-CoA levels in SAT of wt and *Azin2*$^{-/-}$ mice fed for 8 weeks a HFD presented as peak intensity (n = 4–6 mice per group). J, K. EGSEA analysis for KEGG signaling pathways upregulated in *Azin2*$^{-/-}$ mice (J) and GSEA analysis for GO_Positive Regulation of Lipid Storage and REACTOME_Fatty Acyl-CoA Biosynthesis (K) based on bulk RNA-seq in SAT of wt and *Azin2*$^{-/-}$ mice fed for 8 weeks a HFD (n = 4 mice per group). L–N. Relative abundance of TG species (L), lipid groups (M) and ceramide species (N) in SAT of wt and *Azin2*$^{-/-}$ mice fed for 8 weeks a HFD presented as peak intensity, only differentially regulated TG species are shown (n = 5–8 mice per group). TG: Triacylglycerol, Cer: Ceramide, DG: Diacylglycerol, GlcCer: Glucosylceramide, LPC: Lysophosphatidylcholine, PC: Phosphatidylcholine, O-PC: Ether-linked phosphatidylcholine, PE: Phosphatidylethanolamine, PI: Phosphatidylinositol, PS: Phosphatidylserine, SM: Sphingomyelin. O, P. Total and Ki67^{+} AP (PDGFRα^{+}LY6A^{+}CD31^{-}CD45^{-}) abundance per g of tissue in SAT of wt and *Azin2*$^{-/-}$ mice fed for 8 weeks a HFD assessed by flow cytometry (n = 7–9 mice per group). Q. GSEA analysis for REACTOME_Cellular Senescence, HALLMARK_Hypoxia, and REACTOME_Oxidative Stress Induced Senescence pathways based on bulk RNA-seq in SAT of wt and *Azin2*$^{-/-}$ mice fed for 8 weeks a HFD (n = 4 mice per group). R. Percentage of CD9^{high} SAT APs (PDGFRα^{+}LY6A^{+}CD31^{-}CD45^{-}) in wt and *Azin2*$^{-/-}$ mice fed for 8 weeks a HFD (n = 6 mice per group). S–U. scRNA-seq was performed in CD45^{-}CD31^{-} SAT SVF cells of wt and *Azin2*$^{-/-}$ mice fed for 8 weeks a HFD (2 mice pooled per genotype). Down- and up-regulated GO Terms and pathways in *Azin2*$^{-/-}$ versus wt mice plotted according to the –log(adjp) value (S, T). Violin plots showing gene expression scores of *Pparg*, *Cd36*, *Fabp4*, *Apoe*, and *Pltp*, in AP in wt and *Azin2*$^{-/-}$ HFD mice (U). Data in B–I, L–P, R are shown as mean ± SEM. Mann-Whitney *U* test (B, C, F–I, L–P, R) and ANCOVA (D, E) were used for statistical analysis. *p < 0.05, **p < 0.01, ***p < 0.001, ****p < 0.0001. NES: Normalized enrichment score; FDR: False discovery rate.

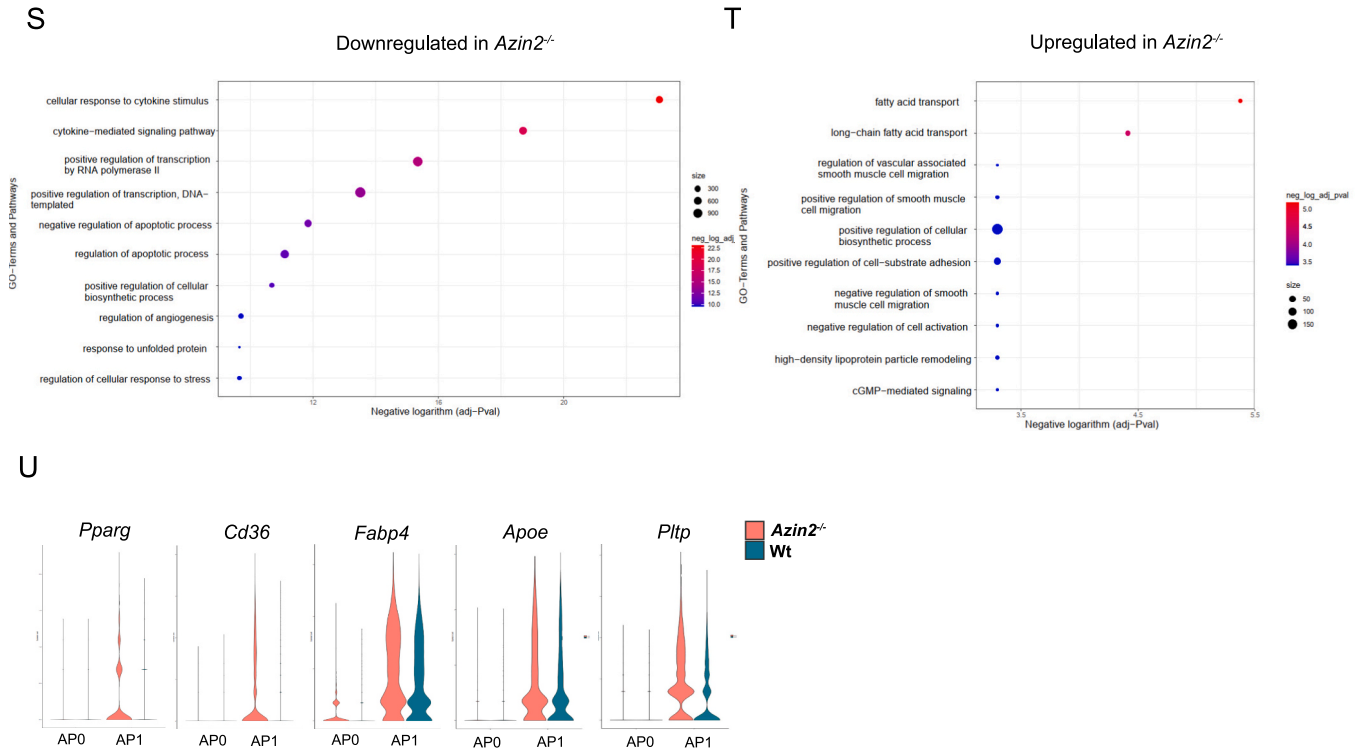

Fig. 6. (*continued*).

In obesity, high AP numbers maintain a healthy adipose tissue by promoting hyperplasia, i.e. formation of many small-sized adipocytes, while low AP numbers associate with adipose tissue hypertrophy, i.e. presence of fewer larger adipocytes (Figs. 1F, S1M) [4,85,93]. AP numbers and numbers of proliferating (Ki67^{+}) APs declined in *Azin2*$^{-/-}$ HFD mice (Fig. 6O, P), as also shown in lean *Azin2*$^{-/-}$ mice (Fig. 5C, D), indicating that AP depletion due to AZIN2 deficiency in the lean state is maintained in obesity. Furthermore, genes related to cellular senescence, hypoxia and oxidative stress-induced senescence were enriched in the SAT of *Azin2*$^{-/-}$ HFD mice (Fig. 6Q). In accordance, cell senescence assessed by β-galactosidase staining (Fig. S8A) and expression of *Cdkn2a* (*p16*) and *Cdkn1a* (*p21*), which encode for negative regulators of cell cycle progression and promote senescence, were increased in *Azin2*$^{-/-}$ SAT APs (Fig. S8B, C) [94,95]. In sum, these data suggest that AZIN2 deficiency leads to loss of APs due to excessive differentiation to adipocytes, reduced proliferation and increased senescence.

We then investigated the impact of AZIN2 deficiency on the transcriptional profile of APs in SAT of HFD-fed mice by scRNA-seq. CD31^{-}CD45^{-} SAT SVF cells of HFD mice consisted of 2 subpopulations, here named AP0 and AP1. Both clusters expressed *Pdgfra* and *Ly6a* (Fig. S9A) validating our FACS (PDGFRα^{+}LY6A^{+}CD31^{-}CD45^{-}) and bead sorting (CD31^{-}CD45^{-}) strategies (see above) and standing in accordance with previous reports [14,16,96–98]. Cluster AP0 selectively expressed early AP markers, such as dipeptidylpeptidase 4 (*Dpp4*), wingless-type MMTV integration site family, member 2 (*Wnt2*), bone morphogenetic protein 7 (*Bmp7*), and peptidase inhibitor 16 (*Pi16*) [13,14,16], as well as dermokine (*Dmkn*) and *Il33* (Fig. S9B), while the AP1 cluster exhibited higher expression of adipogenic genes, such as *Pparg*, *Cd36*, fatty acid binding protein 4 (*Fabp4*), apolipoprotein e (*Apoe*), phospholipid transfer protein (*Pltp*), *Lpl*, coagulation factor III (*F3/Cd142*) and genes encoding proteins linked to ECM remodeling, such as biglycan (*Bgn*), lumican (*Lum*), matrix Gla protein (*Mgp*), *Mmp3* and transforming growth factor beta 1 (*Tgfb1*), compared to AP0 cells (Fig. S9C and Fig. 6U). These data indicated that the AP0 cluster consisted of early progenitors, while AP1 contained committed progenitors. This clustering stands in accordance with previous studies [13–16,98]: AP0 corresponds to P1 of Schwalie et al. [15], ASC2 of Burl et al. [16], group 1 of Merrick et al. [13], FAP3 of Sarvari et al. [98] and mASPC2 of Emont et al. [14], while AP1 corresponds to P2 of Schwalie et al. [15], ASC1 and differentiated ASC of Burl et al. [16], group 2 of Merrick et al. [13], FAP2 of Sarvari et al. [98] and mASPC1 of Emont et al. [14]. These two clusters also correspond to

previously described human AP subpopulations [13,14].

Azin2 was expressed in both AP0 and AP1 (Fig. S9D). Pathway analysis showed that gene expression related to pathways including cellular response to cytokines, gene transcription and negative regulation of apoptosis was downregulated, while gene expression related to lipid metabolism and lipid transport was upregulated in APs of *Azin2*$^{-/-}$ compared to wt mice (Fig. 6S, T). Specifically, expression of *Pparg*, *Cd36*, *Fabp4*, *Apoe* and *Pltp* in the AP1 cluster was upregulated in AZIN2 deficiency (Fig. 6U). In contrast, expression of genes encoding for antioxidant proteins, such as metallothionein 2 (*Mt2*), proteins mediating interactions with the ECM, such as hyaluronan synthase 1 (*Has1*), UDP-glucose 6-dehydrogenase (*Ugdh*), *Cd44* and pentraxin 3 (*Ptx3*), and proteins mediating the response to mitogenic signals, such as immediate early response 5 (*Ier5*) and lamin a (*Lmna*), was downregulated in both clusters in *Azin2*$^{-/-}$ compared to wt mice (Fig. S9E). Notably, expression of *Il4ra*, which was detected only in the AP1 cluster and found to be a negative regulator of adipogenesis and inducer of *Azin2* expression (Figs. 2B, D, E, G–I, S2C, F) [70,71], was decreased in *Azin2*$^{-/-}$ mice (Fig. S9E). This suggests that *Azin2*$^{-/-}$ AP1 cells are less responsive to the anti-adipogenic effects of IL4, which in turn may further accelerate their differentiation to adipocytes (Fig. S9F). Collectively, these data suggest that AZIN2 modulates AP identity, while its deficiency leads to increased AP adipogenic commitment.

Moreover, we mined the GEPIA2 database for expression of genes encoding for progenitor markers in correlation with *AZIN2* expression in human adipose tissue. *AZIN2* mRNA expression correlated with expression of *DPP4*, *WNT2* and *PDGFRA* in both visceral and subcutaneous adipose tissue (Fig. S9G–I, M, N), supporting that *AZIN2* expression demarks AP abundance. *AZIN2* expression also positively correlated with the expression of endothelin receptor type A (*EDNRA*), lin-7 homolog A, crumbs cell polarity complex component (*LIN7A*), alkylglycerol monooxygenase (*AGMO*) and formin homology 2 domain containing 3 (*FHOD3*), which were previously identified as markers of an adipocyte subpopulation with protective function against insulin resistance (Fig. S9J–L, O, P). [14] These correlations collectively suggest that as in the mouse, in humans *AZIN2* expression associates with features of healthy adipose tissue.

BAT function significantly contributes to whole body energy expenditure [99] and polyamine metabolism may regulate BAT function [33,34,100]. Hence, we examined whether AZIN2 deficiency affected BAT morphology, UCP1 expression and expression of other thermogenesis-related genes such *Ppargc1a*, PR domain containing 16 (*Prdm16*), and cytochrome *c* oxidase subunit 8b (*Cox8b*) in BAT [101,102]. Morphology and expression of thermogenic genes were not altered in BAT of *Azin2*$^{-/-}$ compared to wt obese mice (Fig. S10A–C). Of note, as in white APs, *Azin2* expression was also detected in BAT APs (Fig. S10D). Moreover, *Ucp1*, *Ppargc1a*, *Prdm16* and *Cox8b* expression remained unaltered in SAT of *Azin2*$^{-/-}$ compared to wt obese mice (Fig. S10D). These data demonstrate that under the studied experimental conditions, AZIN2 deficiency does not affect brown or 'beige' thermogenesis.

Prolonged obesity leads to steatohepatitis [103]. Hence, we next asked whether AZIN2 deficiency affects liver steatosis in HFD mice. Strikingly, *Azin2*$^{-/-}$ mice fed for 8 weeks a HFD had increased liver weight (Fig. S11A), enhanced steatosis and TG content (Fig. S11B, C), and increased expression of lipogenesis-related genes, such as *Pparg*, *Cebpa*, *Cd36*, *Acaca* and fatty acid synthase (*Fasn*), (Fig. S11D). Expression of inflammatory genes, like *Il6* or *Tnf*, was not altered (not shown). Enhanced liver steatosis in AZIN2 deficient mice could be a consequence of adipose tissue dysfunction promoting ectopic fat accumulation.

3.7. Adipocyte progenitor-specific AZIN2 deficiency

To substantiate the role of AZIN2 in APs, we generated mice with tamoxifen-inducible AP-specific *Azin2* deletion. *Azin2*$^{fl/fl}$ mice were generated by flanking exon 7 of the *Azin2* gene with loxP sites, and they were crossed with *Pdgfra*$^{Cre+ER}$ mice. *Pdgfra*^{CreER};*Azin2*$^{fl/fl}$ mice were treated with tamoxifen for 5 consecutive days by o.g. and feeding with tamoxifen-containing HFD for 3.5 weeks, followed by another 5 weeks of feeding with tamoxifen-free HFD (Fig. 7A). This scheme efficiently deleted *Azin2* in SAT and GAT APs (Figs. 7B, S12A). Strikingly, *Azin2*^{APKO} mice gained more body weight and had impaired glucose tolerance and insulin sensitivity compared to littermate control *Azin2*$^{fl/fl}$ mice (Fig. 7C–E). SAT, GAT, axillary, mesenteric and perirenal adipose tissue weights were increased in *Azin2*^{APKO} compared to *Azin2*$^{fl/fl}$ mice (Figs. 7F, S12B). Accordingly, SAT of *Azin2*^{APKO} mice consisted of larger adipocytes and had reduced *Pdgfra* expression, indicative for fewer APs, compared to SAT of *Azin2*$^{fl/fl}$ mice (Figs. 7G, H, S1G). Finally, GAT of *Azin2*^{APKO} mice presented stronger inflammation, as revealed by elevated expression of *Il6*, *Ccl3* and *Saa3*, and almost significantly increased expression of *Tnf*, *Itgax* and *S100a8* compared to *Azin2*$^{fl/fl}$ mice (Fig. S12C). These findings collectively suggest that AZIN2 in APs plays a key role in regulation of obesity and associated AT inflammation.

4. Discussion

Maintenance of adipose tissue homeostasis requires constant adipocyte renewal through AP differentiation [104]. In periods of increased energy intake or reduced energy expenditure, lipid storage in the adipose tissue protects against ectopic lipid deposition and lipotoxicity; however, excessive adipose tissue expansion leads to adipocyte destruction, hypoxia, inflammation, fibrosis and loss of adipose tissue plasticity, which are associated with the development of dyslipidemia, systemic inflammation and insulin resistance [3,4]. At the start of obesity, APs differentiate to adipocytes, which then grow in size by storing TGs [6,7]. Hence, formation of new adipocytes is necessary for adipose tissue expansion.

While the molecular mechanisms regulating gene transcription during adipogenic differentiation have been dissected in detail [18,105,106], little is known about the cell metabolic circuits orchestrating adipogenesis. Here, we show that polyamine metabolism is downregulated in the adipose tissue upon diet-induced obesity. Components of polyamine metabolism including AZIN2 are expressed in APs and are downregulated upon adipogenic differentiation. On the other hand, type 2 immunity upregulates AZIN2 expression, in keeping with its anti-obesogenic effect [66,70,71]. Accordingly, in the human adipose tissue *AZIN2* mRNA levels positively correlate with expression of type 2 immunity factors.

In young CD-fed mice, AZIN2 deficiency leads to enhanced adipogenesis, reduced AP proliferation and consequently AP depletion, thereby predisposing for development of an unhealthy adipose tissue later in obesity. Hence, we suggest that excessive adipogenesis in the lean/young state causes AP depletion predisposing to aggravated adipose tissue pathophysiology in the context of obesity later in life. Nevertheless, this does not contradict the fact that in established obesity, adipose tissue hyperplasia favors metabolic advantage compared to adipose tissue hypertrophy [4].

Mechanistically, we found that AZIN2 promotes polyamine synthesis and acetylation in APs. Similarly, AZIN2 was recently linked to increased amounts of acetylated polyamines in the brain in tau neuropathy [107]. In accordance, AZIN2 negatively regulates acetyl-CoA amounts in APs and the adipose tissue. Elevated acetyl-CoA amounts in *Azin2*$^{-/-}$ APs can lead to increased histone acetylation and transcription of adipogenic genes, including *Pparg* and *Cebpa* [18]. On the other hand, increased acetyl-CoA amounts in the adipose tissue of *Azin2*$^{-/-}$ mice associate with an altered TG signature, and increased ceramide and DG content, which can drive lipotoxicity, inflammation and insulin resistance [85,88–91,108]. In accordance, *Azin2*$^{-/-}$ HFD-fed mice exhibit increased adipose tissue inflammation and systemic insulin resistance compared to wt HFD mice.

At the single-cell level, AZIN2 deficiency increases gene expression

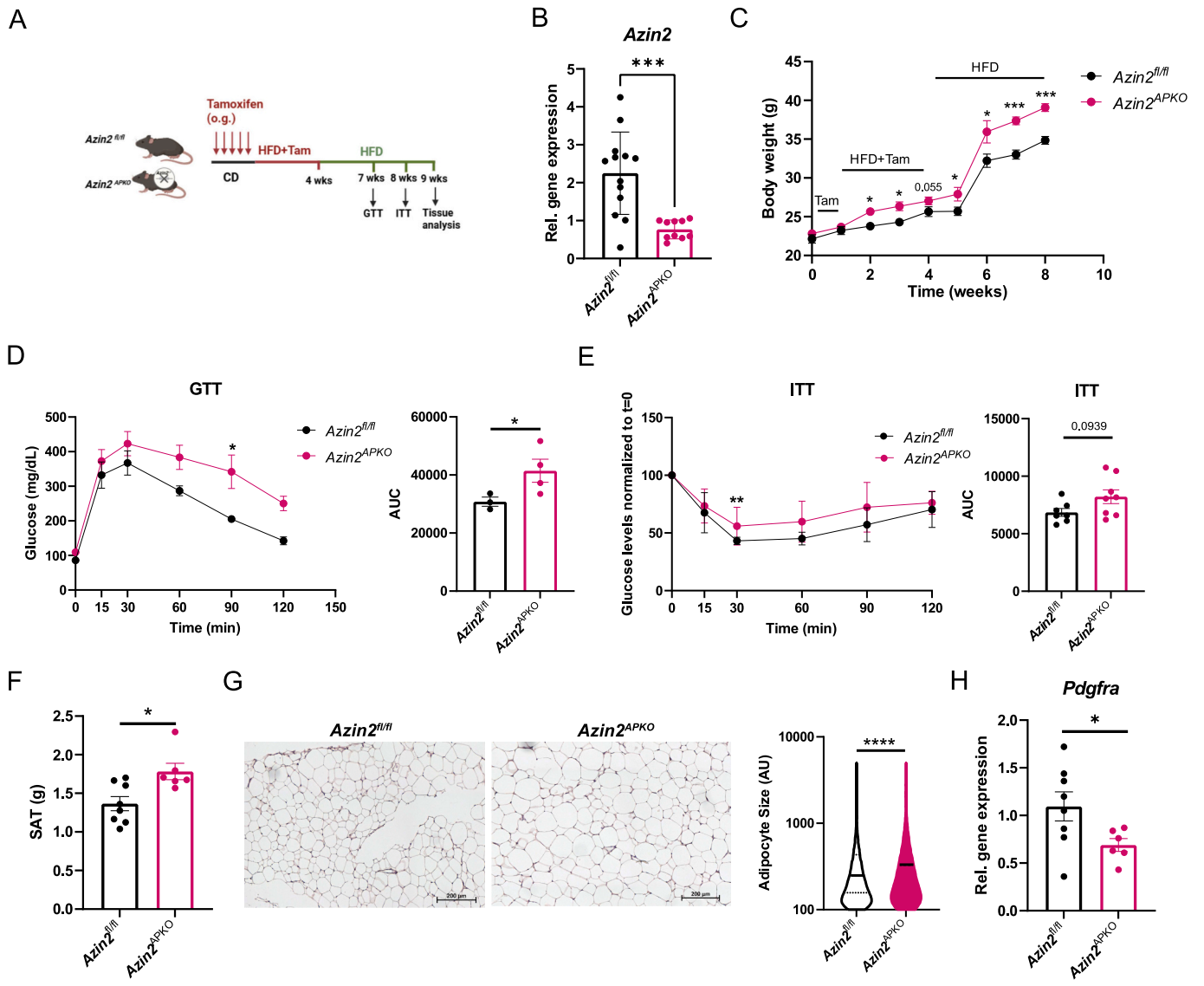

Fig. 7. AP-specific AZIN2 deficiency leads to increased obesity.
A. Experimental setup. B. APs were isolated as CD31^{-}CD45^{-} cells from SAT of *Azin2*$^{fl/fl}$ and *Azin2*^{APKO} mice treated as depicted in (A) and *Azin2* expression was analyzed by qPCR using *18S* as a housekeeping gene (n = 10–13 mice per group). C. Body weight gain in *Azin2*$^{fl/fl}$ and *Azin2*^{APKO} mice (n = 6–8 mice per group). D. GTT performed at week 7 of HFD feeding in *Azin2*$^{fl/fl}$ and *Azin2*^{APKO} mice (n = 3–4 mice per group). Left panel: Blood glucose concentration over time; right panel: area under the curve (AUC). E. ITT performed at week 8 of HFD feeding in *Azin2*$^{fl/fl}$ and *Azin2*^{APKO} mice (n = 7–8 mice per group). Left panel: Blood glucose concentration over time, glucose levels at $t = 0$ were set as 100 %; right panel: AUC. F. SAT weight in *Azin2*$^{fl/fl}$ and *Azin2*^{APKO} mice (n = 6–8 mice per group). G. Left panel: representative images of H&E staining of SAT of *Azin2*$^{fl/fl}$ and *Azin2*^{APKO} mice treated as depicted in (A), scale bar: 200 μm; right panel: adipocyte size quantification (quantification of adipocyte size in one whole SAT piece per mouse in n = 5 mice per group). H. *Pdgfra* relative gene expression in SAT of *Azin2*$^{fl/fl}$ and *Azin2*^{APKO} mice assessed by qPCR using *18S* as a reference gene (n = 6–8 mice per group). Data in B–F, H are shown as mean ± SEM. Mann-Whitney U test was used for statistical analysis. *p < 0.05, **p < 0.01, ***p < 0.001, ****p < 0.0001.

related to adipogenesis and lipid metabolism. *Il4ra* expression is diminished in committed *Azin2*$^{-/-}$ AP (AP1) cells, standing in accordance with its reduction upon adipogenesis, and suggesting that *Azin2*$^{-/-}$ AP1 cells are resistant to the anti-adipogenic effects of IL4, which may further increase their adipogenic differentiation [70,71,109]. Similarly, in human adipose tissue, *AZIN2* expression positively correlates with early progenitor and type 2 immunity markers. To which extent AZIN2 plays a protective role in human obesity should be examined in future studies.

Furthermore, AZIN2 was found to maintain a 'healthy' AP state as its deficiency predisposes to reduced AP numbers and increased AP senescence. Accordingly, genes related to senescence presented increased histone acetylation in *Azin2*$^{-/-}$ APs. Previous reports showed that polyamine depletion leads to hyperacetylation, ROS generation and necrosis, while spermidine treatment induces H3 deacetylation through inhibition of histone acetyltransferases and suppresses oxidative stress [21]. Accordingly, we show that polyamines decrease acetyl-CoA amounts in APs by fueling their acetylation. In concert with our findings, SAT1, the enzyme mediating polyamine acetylation, was previously shown to be a regulator of acetyl-CoA levels in adipose tissue, and SAT1 knockout increased body fat in HFD-fed mice [110–114].

Moreover, spermidine and spermine were previously shown to protect against diet-induced obesity and associated metabolic disturbances [33,115–119]. Along these lines, we show that spermidine inhibits adipogenesis in an AZIN2-dependent manner, suggesting that spermidine acetylation and not spermidine per se downregulates adipogenesis. Spermidine also promotes autophagy, mitophagy and mitochondrial respiration in cardiomyocytes, thereby providing cardioprotection [22],

while it inhibits oxidative stress and extends the lifespan of cells and organisms spanning from yeast and worms to mice and humans [21,22,120]. Recently, spermidine was shown to activate fatty acid oxidation in $CD8^+$ T cells through direct binding to and activation of mitochondrial trifunctional protein (MTP) [121]. In accordance, we show that AZIN2 preserves gene expression related to mitochondrial metabolism, i.e. citrate cycle function, oxidative phosphorylation and lipid oxidation, and reduces gene expression related to oxidative stress in the adipose tissue of obese mice. Whether AZIN2 also counteracts aging and extends the lifespan of cells and organisms merits further investigation.

The characteristics of different adipose tissue depots can vary significantly depending on the anatomical position. In humans, APs are more abundant in gluteofemoral compared to abdominal subcutaneous and omental adipose tissue [122]. This is in agreement with the rather hyperplastic nature of gluteofemoral subcutaneous compared to visceral adipose tissue and the metabolically favorable fat deposition at the gluteofemoral area compared to the visceral site [4]. On the other hand, adipose tissue hyperplasia in gonadal and inguinal subcutaneous adipose tissue differs in males and females [6,7,12]. Sex-dependent adaptations of polyamine metabolism or other cell metabolic circuits in different adipose tissue depots is an important open question.

In conclusion, this study introduces AZIN2 as a novel marker of APs. AZIN2 regulates acetyl-CoA amounts and transcriptional networks that determine AP fate, while inactivation of AZIN2 depletes APs leading to aggravated obesity, dysmetabolism and inflammation. These findings expand the current knowledge on adipose tissue (patho)physiology and link obesity and associated morbidities with polyamine metabolism in APs. Future studies should address the role of polyamine metabolism in human obesity and its modulation by factors with translational potential.

Supplementary data to this article can be found online at https://doi.org/10.1016/j.metabol.2025.156358.

CRediT authorship contribution statement

Christine Mund: Investigation. **Anupam Sinha:** Software, Formal analysis, Data curation. **Anika Aderhold:** Validation, Methodology, Investigation. **Ivona Mateska:** Validation, Methodology, Investigation. **Eman Hagag:** Investigation. **Sofia Traikov:** Methodology, Investigation, Data curation. **Bettina Gercken:** Investigation. **Andres Soto:** Investigation. **Jonathan Pollock:** Investigation. **Lilli Arndt:** Investigation. **Michele Wölk:** Investigation, Formal analysis, Data curation. **Natalie Werner:** Investigation. **Georgia Fodelianaki:** Investigation. **Pallavi Subramanian:** Investigation. **Kyoung-Jin Chung:** Methodology. **Sylvia Grosskklaus:** Investigation. **Mathias Langner:** Investigation. **Mohamed Elgendy:** Resources. **Tatyana Grinenko:** Resources. **Ben Wielockx:** Resources. **Andreas Dahl:** Software, Formal analysis. **Martin Gericke:** Resources. **Matthias Blüher:** Writing – review & editing. **Ünal Coskun:** Resources. **David Voehringer:** Resources. **Maria Fedorova:** Resources. **Mirko Peitzsch:** Resources, Formal analysis, Data curation. **Peter J. Murray:** Writing – review & editing, Methodology. **Triantafyllos Chavakis:** Writing – review & editing, Resources, Funding acquisition, Conceptualization. **Vasileia Ismini Alexaki:** Writing – review & editing, Writing – original draft, Validation, Supervision, Resources, Project administration, Funding acquisition, Data curation, Conceptualization.

Funding

This work was supported by funds from the Deutsche Forschungsgemeinschaft (AL 1686/6-1, SFB-TRR 205 project A07 to VIA, SFB-TRR 412 project B08 to VIA and MF, and SFB-TRR 127 to TC), the Saxon State Ministry of Science, Culture, and Tourism-SMWK (Unterstützung profilbestimmender Struktureinheiten der TUD to TC) and TG70 by Sächsische Aufbaubank and SMWK (the measure is cofinanced with tax funds on the basis of the budget passed by the Saxon State Parliament) to MF. TC is supported by an ERC grant (LOSYSINCHRON). The graphical abstract and schemes were created with BioRender.

Declaration of competing interest

The authors declare that they have no known competing financial interests or personal relationships that could have appeared to influence the work reported in this paper.

Acknowledgments

We thank the Core Facility Cellular Imaging of the Medical Faculty Carl Gustav Carus, TU Dresden, especially Michael Gerlach, for the technical support. We also thank Peter Mirtschink (Institute of Clinical Chemistry and Laboratory Medicine, Faculty of Medicine and University Hospital Carl Gustav Carus, Technische Universität Dresden, Dresden, Germany) for his contribution regarding metabolomics.

Data availability•

All data presented in the study will be shared by the lead contact upon request.

The bulk RNA-seq, ChIP-seq and scRNA-seq data reported in this paper are accessible in the reference Series GSE235012 under the link https://www.ncbi.nlm.nih.gov/geo/query/acc.cgi?acc=GSE235012.•

Any additional data is available from the corresponding author upon request.

References

[1] Bluher M. Obesity: global epidemiology and pathogenesis. Nat Rev Endocrinol 2019;15:288–98.
[2] Ghaben AL, Scherer PE. Adipogenesis and metabolic health. Nat Rev Mol Cell Biol 2019;20:242–58.
[3] Chavakis T, Alexaki VI, Ferrante Jr AW. Macrophage function in adipose tissue homeostasis and metabolic inflammation. Nat Immunol 2023;24(5):757–66.
[4] Sakers A, De Siqueira MK, Seale P, Villanueva CJ. Adipose-tissue plasticity in health and disease. Cell 2022;185:419–46.
[5] Wang QA, Tao C, Gupta RK, Scherer PE. Tracking adipogenesis during white adipose tissue development, expansion and regeneration. Nat Med 2013;19:1338–44.
[6] Jeffery E, Church CD, Holtrup B, Colman L, Rodeheffer MS. Rapid depot-specific activation of adipocyte precursor cells at the onset of obesity. Nat Cell Biol 2015;17:376–85.
[7] Jeffery E, Wing A, Holtrup B, Sebo Z, Kaplan JL, Saavedra-Pena R, et al. The adipose tissue microenvironment regulates depot-specific adipogenesis in obesity. Cell Metab 2016;24:142–50.
[8] Arner P, Andersson DP, Thorne A, Wiren M, Hoffstedt J, Naslund E, et al. Variations in the size of the major omentum are primarily determined by fat cell number. J Clin Endocrinol Metab 2013;98:E897–901.
[9] Buchwald LM, Neess D, Hansen D, Doktor TK, Ramesh V, Steffensen LB, et al. Body weight control via protein kinase CK2: diet-induced obesity counteracted by pharmacological targeting. Metabolism 2025;162:156060.
[10] Zhang T, Ren Z, Mao R, Yi W, Wang B, Yang H, et al. LINC00278 and BRG1: a key regulatory axis in male obesity and preadipocyte adipogenesis. Metabolism 2025;168:156194.
[11] Lee YH, Petkova AP, Mottillo EP, Granneman JG. In vivo identification of bipotential adipocyte progenitors recruited by beta3-adrenoceptor activation and high-fat feeding. Cell Metab 2012;15:480–91.
[12] Cattaneo P, Mukherjee D, Spinozzi S, Zhang L, Larcher V, Stallcup WB, et al. Parallel lineage-tracing studies establish fibroblasts as the prevailing in vivo adipocyte progenitor. Cell Rep 2020;30(571–82):e2.
[13] Merrick D, Sakers A, Irgebay Z, Okada C, Calvert C, Morley MP, et al. Identification of a mesenchymal progenitor cell hierarchy in adipose tissue. Science 2019;364.
[14] Emont MP, Jacobs C, Essene AL, Pant D, Tenen D, Colleluori G, et al. A single-cell atlas of human and mouse white adipose tissue. Nature 2022;603:926–33.
[15] Schwalie PC, Dong H, Zachara M, Russeil J, Alpern D, Akchiche N, et al. A stromal cell population that inhibits adipogenesis in mammalian fat depots. Nature 2018;559:103–8.
[16] Burl RB, Ramseyer VD, Rondini EA, Pique-Regi R, Lee YH, Granneman JG. Deconstructing adipogenesis induced by beta3-adrenergic receptor activation with single-cell expression profiling. Cell Metab 2018;28(300–9):e4.

[17] Hepler C, Shan B, Zhang Q, Henry GH, Shao M, Vishvanath L, et al. Identification of functionally distinct fibro-inflammatory and adipogenic stromal subpopulations in visceral adipose tissue of adult mice. Elife 2018:7.
[18] Siersbaek R, Nielsen R, Mandrup S. Transcriptional networks and chromatin remodeling controlling adipogenesis. Trends Endocrinol Metab 2012;23:56–64.
[19] Michael AJ. Polyamines in eukaryotes, bacteria, and archaea. J Biol Chem 2016; 291:14896–903.
[20] Rieck J, Skatchkov SN, Derst C, Eaton MJ, Veh RW. Unique chemistry, intake, and metabolism of polyamines in the Central Nervous System (CNS) and its body. Biomolecules 2022:12.
[21] Eisenberg T, Knauer H, Schauer A, Buttner S, Ruckenstuhl C, Carmona-Gutierrez D, et al. Induction of autophagy by spermidine promotes longevity. Nat Cell Biol 2009;11:1305–14.
[22] Eisenberg T, Abdellatif M, Schroeder S, Primessnig U, Stekovic S, Pendl T, et al. Cardioprotection and lifespan extension by the natural polyamine spermidine. Nat Med 2016;22:1428–38.
[23] Lee CY, Su GC, Huang WY, Ko MY, Yeh HY, Chang GD, et al. Promotion of homology-directed DNA repair by polyamines. Nat Commun 2019;10:65.
[24] D'Agostino L, Di Luccia A. Polyamines interact with DNA as molecular aggregates. Eur J Biochem 2002;269:4317–25.
[25] Kahana C. The antizyme family for regulating polyamines. J Biol Chem 2018;293: 18730–5.
[26] Pegg AE. Functions of polyamines in mammals. J Biol Chem 2016;291:14904–12.
[27] Pisani DF, Lettieri-Barbato D, Ivanov S. Polyamine metabolism in macrophage-adipose tissue function and homeostasis. Trends Endocrinol Metab 2024;35: 937–50.
[28] Kramer DL, Diegelman P, Jell J, Vujcic S, Merali S, Porter CW. Polyamine acetylation modulates polyamine metabolic flux, a prelude to broader metabolic consequences. J Biol Chem 2008;283:4241–51.
[29] Ramos-Molina B, Lambertos A, Penafiel R. Antizyme inhibitors in polyamine metabolism and beyond: physiopathological implications. Med Sci (Basel) 2018: 6.
[30] Wu HY, Chen SF, Hsieh JY, Chou F, Wang YH, Lin WT, et al. Structural basis of antizyme-mediated regulation of polyamine homeostasis. Proc Natl Acad Sci U S A 2015;112:11229–34.
[31] Kraus D, Yang Q, Kong D, Banks AS, Zhang L, Rodgers JT, et al. Nicotinamide N-methyltransferase knockdown protects against diet-induced obesity. Nature 2014; 508:258–62.
[32] Monelli E, Villacampa P, Zabala-Letona A, Martinez-Romero A, Llena J, Beiroa D, et al. Angiocrine polyamine production regulates adiposity. Nat Metab 2022;4: 327–43.
[33] Ma L, Ni Y, Hu L, Zhao Y, Zheng L, Yang S, et al. Spermidine ameliorates high-fat diet-induced hepatic steatosis and adipose tissue inflammation in preexisting obese mice. Life Sci 2021;265:118739.
[34] Ni Y, Zheng L, Zhang L, Li J, Pan Y, Du H, et al. Spermidine activates adipose tissue thermogenesis through autophagy and fibroblast growth factor 21. J Nutr Biochem 2024;125:109569.
[35] Ramos-Molina B, Queipo-Ortuno MI, Lambertos A, Tinahones FJ, Penafiel R. Dietary and gut microbiota polyamines in obesity- and age-related diseases. Front Nutr 2019;6:24.
[36] Chung KJ, Chatzigeorgiou A, Economopoulou M, Garcia-Martin R, Alexaki VI, Mitroulis I, et al. A self-sustained loop of inflammation-driven inhibition of beige adipogenesis in obesity. Nat Immunol 2017;18:654–64.
[37] Garcia-Martin R, Alexaki VI, Qin N, Rubin de Celis MF, Economopoulou M, Ziogas A, et al. Adipocyte-specific hypoxia-inducible factor 2alpha deficiency exacerbates obesity-induced brown adipose tissue dysfunction and metabolic dysregulation. Mol Cell Biol 2016;36:376–93.
[38] Finkelman FD, Madden KB, Morris SC, Holmes JM, Boiani N, Katona IM, et al. Anti-cytokine antibodies as carrier proteins. Prolongation of in vivo effects of exogenous cytokines by injection of cytokine-anti-cytokine antibody complexes. J Immunol 1993;151:1235–44.
[39] Lee MW, Odegaard JI, Mukundan L, Qiu Y, Molofsky AB, Nussbaum JC, et al. Activated type 2 innate lymphoid cells regulate beige fat biogenesis. Cell 2015; 160:74–87.
[40] Thuma N, Dohler D, Mielenz D, Sticht H, Radtke D, Reimann L, et al. A newly identified secreted larval antigen elicits basophil-dependent protective immunity against N. brasiliensis infection. Front Immunol 2022;13:979491.
[41] Thangapandi VR, Knittelfelder O, Brosch M, Patsenker E, Vvedenskaya O, Buch S, et al. Loss of hepatic Mboat7 leads to liver fibrosis. Gut 2021;70:940–50.
[42] Alexaki VI, Fodelianaki G, Neuwirth A, Mund C, Kourgiantaki A, Ieronimaki E, et al. DHEA inhibits acute microglia-mediated inflammation through activation of the TrkA-Akt1/2-CREB-Jmjd3 pathway. Mol Psychiatry 2018;23:1410–20.
[43] Witt A, Mateska I, Palladini A, Sinha A, Woelk M, Harauma A, et al. Fatty acid desaturase 2 determines the lipidomic landscape and steroidogenic function of the adrenal gland. Sci Adv 2023;9(29):eadf6710.
[44] Mateska I, Witt A, Hagag E, Sinha A, Yilmaz C, Thanou E, et al. Inflammation-induced downregulation of succinate dehydrogenase regulates adrenocortical function. Elife 2023;12:e83064. Jul 14.
[45] Martin M. Cutadept removes adapter sequences from high-throughput sequncing reads. EMBnetjournal 2011;7:2803–9.
[46] Dobin A, Davis CA, Schlesinger F, Drenkow J, Zaleski C, Jha S, et al. STAR: ultrafast universal RNA-seq aligner. Bioinformatics 2013;29:15–21.
[47] Anders S, Pyl PT, Huber W. HTSeq—a Python framework to work with high-throughput sequencing data. Bioinformatics 2015;31:166–9.
[48] Anders S, Huber W. Differential expression analysis for sequence count data. Genome Biol 2010;11:R106.
[49] Subramanian A, Tamayo P, Mootha VK, Mukherjee S, Ebert BL, Gillette MA, et al. Gene set enrichment analysis: a knowledge-based approach for interpreting genome-wide expression profiles. Proc Natl Acad Sci U S A 2005;102:15545–50.
[50] Alhamdoosh M, Ng M, Wilson NJ, Sheridan JM, Huynh H, Wilson MJ, et al. Combining multiple tools outperforms individual methods in gene set enrichment analyses. Bioinformatics 2017;33:414–24.
[51] Hao Y, Hao S, Andersen-Nissen E, Mauck 3rd WM, Zheng S, Butler A, et al. Integrated analysis of multimodal single-cell data. Cell 2021;184:3573–87. e29.
[52] Xie Z, Bailey A, Kuleshov MV, Clarke DJB, Evangelista JE, Jenkins SL, et al. Gene set knowledge discovery with Enrichr. Curr Protoc 2021;1:e90.
[53] Ewels PA, Peltzer A, Fillinger S, Patel H, Alneberg J, Wilm A, et al. The nf-core framework for community-curated bioinformatics pipelines. Nat Biotechnol 2020;38:276–8.
[54] Quinlan AR, Hall IM. BEDTools: a flexible suite of utilities for comparing genomic features. Bioinformatics 2010;26:841–2.
[55] Liao Y, Smyth GK, Shi W. featureCounts: an efficient general purpose program for assigning sequence reads to genomic features. Bioinformatics 2014;30:923–30.
[56] Raudvere U, Kolberg L, Kuzmin I, Arak T, Adler P, Peterson H, et al. g:Profiler: a web server for functional enrichment analysis and conversions of gene lists (2019 update). Nucleic Acids Res 2019;47:W191–8.
[57] Robinson JT, Thorvaldsdottir H, Winckler W, Guttman M, Lander ES, Getz G, et al. Integrative genomics viewer. Nat Biotechnol 2011;29:24–6.
[58] Ramirez F, Ryan DP, Gruning B, Bhardwaj V, Kilpert F, Richter AS, et al. deepTools2: a next generation web server for deep-sequencing data analysis. Nucleic Acids Res 2016;44:W160–5.
[59] Langner M, Mateska I, Bechmann N, Wielockx B, Chavakis T, Alexaki VI, et al. Liquid chromatography-tandem mass spectrometry based quantification of arginine metabolites including polyamines in different sample matrices. J Chromatogr A 2022;1671:463021.
[60] Lange M, Angelidou G, Ni Z, Criscuolo A, Schiller J, Bluher M, et al. AdipoAtlas: a reference lipidome for human white adipose tissue. Cell Rep Med 2021;2:100407.
[61] Goracci L, Tortorella S, Tiberi P, Pellegrino RM, Di Veroli A, Valeri A, et al. Lipostar, a comprehensive platform-neutral cheminformatics tool for lipidomics. Anal Chem 2017;89:6257–64.
[62] Lavrynenko O, Rodenfels J, Carvalho M, Dye NA, Lafont R, Eaton S, et al. The ecdysteroidome of Drosophila: influence of diet and development. Development 2015;142:3758–68.
[63] Schindelin J, Arganda-Carreras I, Frise E, Kaynig V, Longair M, Pietzsch T, et al. Fiji: an open-source platform for biological-image analysis. Nat Methods 2012;9: 676–82.
[64] Michailidou Z, Gomez-Salazar M, Alexaki VI. Innate immune cells in the adipose tissue in health and metabolic disease. J Innate Immun 2022;14:4–30.
[65] Wu D, Molofsky AB, Liang HE, Ricardo-Gonzalez RR, Jouihan HA, Bando JK, et al. Eosinophils sustain adipose alternatively activated macrophages associated with glucose homeostasis. Science 2011;332:243–7.
[66] Brestoff JR, Artis D. Immune regulation of metabolic homeostasis in health and disease. Cell 2015;161:146–60.
[67] Closs EI, Boissel JP, Habermeier A, Rotmann A. Structure and function of cationic amino acid transporters (CATs). J Membr Biol 2006;213:67–77.
[68] Murray PJ. Macrophage polarization. Annu Rev Physiol 2017;79:541–66.
[69] LaPorte SL, Juo ZS, Vaclavikova J, Colf LA, Qi X, Heller NM, et al. Molecular and structural basis of cytokine receptor pleiotropy in the interleukin-4/13 system. Cell 2008;132:259–72.
[70] Ying T, Golden T, Cheng L, Ishibashi J, Seale P, Simmons RA. Neonatal IL-4 exposure decreases adipogenesis of male rats into adulthood. Am J Physiol Endocrinol Metab 2021;320:E1148–57.
[71] Tsao CH, Shiau MY, Chuang PH, Chang YH, Hwang J. Interleukin-4 regulates lipid metabolism by inhibiting adipogenesis and promoting lipolysis. J Lipid Res 2014;55:385–97.
[72] Voehringer D, Shinkai K, Locksley RM. Type 2 immunity reflects orchestrated recruitment of cells committed to IL-4 production. Immunity 2004;20:267–77.
[73] Tang Z, Kang B, Li C, Chen T, Zhang Z. GEPIA2: an enhanced web server for large-scale expression profiling and interactive analysis. Nucleic Acids Res 2019;47: W556–60.
[74] Lopez-Contreras AJ, Ramos-Molina B, Cremades A, Penafiel R. Antizyme inhibitor 2 (AZIN2/ODCp) stimulates polyamine uptake in mammalian cells. J Biol Chem 2008;283:20761–9.
[75] Kanerva K, Makitie LT, Pelander A, Heiskala M, Andersson LC. Human ornithine decarboxylase paralogue (ODCp) is an antizyme inhibitor but not an arginine decarboxylase. Biochem J 2008;409:187–92.
[76] Puleston DJ, Buck MD, Klein Geltink RI, Kyle RL, Caputa G, O'Sullivan D, et al. Polyamines and eIF5A hypusination modulate mitochondrial respiration and macrophage activation. Cell Metab 2019;30(352–63):e8.
[77] Zhou J, Pang J, Tripathi M, Ho JP, Widjaja AA, Shekeran SG, et al. Spermidine-mediated hypusination of translation factor EIF5A improves mitochondrial fatty acid oxidation and prevents non-alcoholic steatohepatitis progression. Nat Commun 2022;13:5202.
[78] Anderson-Baucum E, Pineros AR, Kulkarni A, Webb-Robertson BJ, Maier B, Anderson RM, et al. Deoxyhypusine synthase promotes a pro-inflammatory macrophage phenotype. Cell Metab 2021;33:1883–93. e7.
[79] Fung TS, Ryu KW, Thompson CB. Arginine: at the crossroads of nitrogen metabolism. EMBO J 2025;44:1275–93.
[80] Pietrocola F, Galluzzi L, Bravo-San Pedro JM, Madeo F, Kroemer G. Acetyl coenzyme A: a central metabolite and second messenger. Cell Metab 2015;21: 805–21.

[81] Matsumura Y, Ito R, Yajima A, Yamaguchi R, Tanaka T, Kawamura T, et al. Spatiotemporal dynamics of SETD5-containing NCoR-HDAC3 complex determines enhancer activation for adipogenesis. Nat Commun 2021;12:7045.
[82] Calo E, Wysocka J. Modification of enhancer chromatin: what, how, and why? Mol Cell 2013;49:825–37.
[83] Zhang Q, Ramlee MK, Brunmeir R, Villanueva CJ, Halperin D, Xu F. Dynamic and distinct histone modifications modulate the expression of key adipogenesis regulatory genes. Cell Cycle 2012;11:4310–22.
[84] Steger DJ, Grant GR, Schupp M, Tomaru T, Lefterova MI, Schug J, et al. Propagation of adipogenic signals through an epigenomic transition state. Genes Dev 2010;24:1035–44.
[85] Vegiopoulos A, Rohm M, Herzig S. Adipose tissue: between the extremes. EMBO J 2017;36:1999–2017.
[86] Marcelin G, Ferreira A, Liu Y, Atlan M, Aron-Wisnewsky J, Pelloux V, et al. A PDGFRalpha-mediated switch toward CD9(high) adipocyte progenitors controls obesity-induced adipose tissue fibrosis. Cell Metab 2017;25:673–85.
[87] Grzybek M, Palladini A, Alexaki VI, Surma MA, Simons K, Chavakis T, et al. Comprehensive and quantitative analysis of white and brown adipose tissue by shotgun lipidomics. Mol Metab 2019;22:12–20.
[88] Kojta I, Chacinska M, Blachnio-Zabielska A. Obesity, bioactive lipids, and adipose tissue inflammation in insulin resistance. Nutrients 2020;12.
[89] Lyu K, Zhang Y, Zhang D, Kahn M, Ter Horst KW, Rodrigues MRS, et al. A membrane-bound diacylglycerol species induces PKCε-mediated hepatic insulin resistance. Cell Metab 2020;32:654–64. e5.
[90] Chaurasia B, Kaddai VA, Lancaster GI, Henstridge DC, Sriram S, Galam DL, et al. Adipocyte ceramides regulate subcutaneous adipose browning, inflammation, and metabolism. Cell Metab 2016;24:820–34.
[91] Turpin SM, Nicholls HT, Willmes DM, Mourier A, Brodesser S, Wunderlich CM, et al. Obesity-induced CerS6-dependent C16:0 ceramide production promotes weight gain and glucose intolerance. Cell Metab 2014;20:678–86.
[92] Turpin-Nolan SM, Hammerschmidt P, Chen W, Jais A, Timper K, Awazawa M, et al. CerS1-derived C(18:0) ceramide in skeletal muscle promotes obesity-induced insulin resistance. Cell Rep 2019;26:1–10. e7.
[93] Bauza-Thorbrugge M, Vujicic M, Chanclon B, Palsdottir V, Pillon NJ, Benrick A, et al. Adiponectin stimulates Sca1(+)CD34(−)-adipocyte precursor cells associated with hyperplastic expansion and beiging of brown and white adipose tissue. Metabolism 2024;151:155716.
[94] Lopez-Dominguez JA, Rodriguez-Lopez S, Ahumada-Castro U, Desprez PY, Konovalenko M, Laberge RM, et al. Cdkn1a transcript variant 2 is a marker of aging and cellular senescence. Aging (Albany NY) 2021;13:13380–92.
[95] Salama R, Sadaie M, Hoare M, Narita M. Cellular senescence and its effector programs. Genes Dev 2014;28:99–114.
[96] Rodeheffer MS, Birsoy K, Friedman JM. Identification of white adipocyte progenitor cells in vivo. Cell 2008;135:240–9.
[97] Lee YH, Petkova AP, Granneman JG. Identification of an adipogenic niche for adipose tissue remodeling and restoration. Cell Metab 2013;18:355–67.
[98] Sarvari AK, Van Hauwaert EL, Markussen LK, Gammelmark E, Marcher AB, Ebbesen MF, et al. Plasticity of epididymal adipose tissue in response to diet-induced obesity at single-nucleus resolution. Cell Metab 2021;33:437–53. e5.
[99] Chouchani ET, Kazak L, Spiegelman BM. New advances in adaptive thermogenesis: UCP1 and beyond. Cell Metab 2019;29:27–37.
[100] Yuan F, Zhang L, Cao Y, Gao W, Zhao C, Fang Y, et al. Spermidine/spermine N1-acetyltransferase-mediated polyamine catabolism regulates beige adipocyte biogenesis. Metabolism 2018;85:298–304.
[101] Das A, Mund C, Hagag E, Garcia-Martin R, Karadima E, Witt A, et al. Adenylate cyclase 10 promotes brown adipose tissue thermogenesis. iScience 2025;28:111833.
[102] Alexaki VI, Chavakis T. The role of innate immunity in the regulation of brown and beige adipogenesis. Rev Endocr Metab Disord 2016;17:41–9.
[103] Suzuki A, Diehl AM. Nonalcoholic steatohepatitis. Annu Rev Med 2017;68:85–98.
[104] Spalding KL, Arner E, Westermark PO, Bernard S, Buchholz BA, Bergmann O, et al. Dynamics of fat cell turnover in humans. Nature 2008;453:783–7.
[105] Rauch A, Mandrup S. Transcriptional networks controlling stromal cell differentiation. Nat Rev Mol Cell Biol 2021;22:465–82.
[106] Shukla V, Cetnarowska A, Hyldahl M, Mandrup S. Interplay between regulatory elements and chromatin topology in cellular lineage determination. Trends Genet 2022;38:1048–61.
[107] Sandusky-Beltran LA, Kovalenko A, Placides DS, Ratnasamy K, Ma C, Hunt Jr JB, et al. Aberrant AZIN2 and polyamine metabolism precipitates tau neuropathology. J Clin Invest 2021;131.
[108] Xia JY, Holland WL, Kusminski CM, Sun K, Sharma AX, Pearson MJ, et al. Targeted induction of ceramide degradation leads to improved systemic metabolism and reduced hepatic steatosis. Cell Metab 2015;22:266–78.
[109] Shiau MY, Chuang PH, Yang CP, Hsiao CW, Chang SW, Chang KY, et al. Mechanism of interleukin-4 reducing lipid deposit by regulating hormone-sensitive lipase. Sci Rep 2019;9:11974.
[110] Jell J, Merali S, Hensen ML, Mazurchuk R, Spernyak JA, Diegelman P, et al. Genetically altered expression of spermidine/spermine N1-acetyltransferase affects fat metabolism in mice via acetyl-CoA. J Biol Chem 2007;282:8404–13.
[111] Liu C, Perez-Leal O, Barrero C, Zahedi K, Soleimani M, Porter C, et al. Modulation of polyamine metabolic flux in adipose tissue alters the accumulation of body fat by affecting glucose homeostasis. Amino Acids 2014;46:701–15.
[112] Pirinen E, Kuulasmaa T, Pietila M, Heikkinen S, Tusa M, Itkonen P, et al. Enhanced polyamine catabolism alters homeostatic control of white adipose tissue mass, energy expenditure, and glucose metabolism. Mol Cell Biol 2007;27:4953–67.
[113] Pietrocola F, Castoldi F, Madeo F, Kroemer G. Triethylenetetramine (trientine): a caloric restriction mimetic with a new mode of action. Autophagy 2020;16:1534–6.
[114] Castoldi F, Hyvonen MT, Durand S, Aprahamian F, Sauvat A, Malik SA, et al. Chemical activation of SAT1 corrects diet-induced metabolic syndrome. Cell Death Differ 2020;27:2904–20.
[115] Ma L, Ni Y, Wang Z, Tu W, Ni L, Zhuge F, et al. Spermidine improves gut barrier integrity and gut microbiota function in diet-induced obese mice. Gut Microbes 2020;12:1–19.
[116] Sadasivan SK, Vasamsetti B, Singh J, Marikunte VV, Oommen AM, Jagannath MR, et al. Exogenous administration of spermine improves glucose utilization and decreases bodyweight in mice. Eur J Pharmacol 2014;729:94–9.
[117] Liao CY, Kummert OMP, Bair AM, Alavi N, Alavi J, Miller DM, et al. The autophagy inducer spermidine protects against metabolic dysfunction during overnutrition. J Gerontol A Biol Sci Med Sci 2021;76:1714–25.
[118] Wang D, Yin J, Zhou Z, Tao Y, Jia Y, Jie H, et al. Oral spermidine targets brown fat and skeletal muscle to mitigate diet-induced obesity and metabolic disorders. Mol Nutr Food Res 2021;65:e2100315.
[119] Nakatani S, Horimoto Y, Nakabayashi N, Karasawa M, Wada M, Kobata K. Spermine suppresses adipocyte differentiation and exerts anti-obesity effects in vitro and in vivo. Int J Mol Sci 2022;23.
[120] Madeo F, Eisenberg T, Pietrocola F, Kroemer G. Spermidine in health and disease. Science 2018;359.
[121] Al-Habsi M, Chamoto K, Matsumoto K, Nomura N, Zhang B, Sugiura Y, et al. Spermidine activates mitochondrial trifunctional protein and improves antitumor immunity in mice. Science 2022;378:eabj3510.
[122] Raajendiran A, Ooi G, Bayliss J, O'Brien PE, Schittenhelm RB, Clark AK, et al. Identification of metabolically distinct adipocyte progenitor cells in human adipose tissues. Cell Rep 2019;27:1528–40. e7.